



The Sloan Digital Sky Survey Reverberation Mapping Project: UV–Optical Accretion Disk Measurements with the Hubble Space Telescope

Y. Homayouni^{1,2} , Megan R. Sturm^{1,3} , Jonathan R. Trump¹ , Keith Horne⁴ , C. J. Grier⁵ , Yue Shen^{6,7} , W. N. Brandt^{8,9,10} , Gloria Fonseca Alvarez¹, P. B. Hall¹¹ , Luis C. Ho^{12,13} , Jennifer I-Hsiu Li^{6,14} , Mouyuan Sun¹⁵ , and

D. P. Schneider^{8,9}

¹ Department of Physics, University of Connecticut, 2152 Hillside Road, Unit 3046, Storrs, CT 06269-3046, USA; yhomayouni@stsci.edu

² Space Telescope Science Institute, 3700 San Martin Drive, Baltimore, MD 21218, USA

³ Department of Physics, Montana State University, Bozeman, MT 59717, USA

⁴ SUPA Physics and Astronomy, University of St. Andrews, Fife, KY16 9SS, Scotland, UK

⁵ Steward Observatory, The University of Arizona, 933 North Cherry Avenue, Tucson, AZ 85721, USA

⁶ Department of Astronomy, University of Illinois at Urbana-Champaign, Urbana, IL, 61801, USA

⁷ National Center for Supercomputing Applications, University of Illinois at Urbana-Champaign, Urbana, IL, 61801, USA

⁸ Department of Astronomy and Astrophysics, The Pennsylvania State University, 525 Davey Laboratory, University Park, PA 16802, USA

⁹ Institute for Gravitation and the Cosmos, The Pennsylvania State University, University Park, PA 16802, USA

¹⁰ Department of Physics, 104 Davey Lab, The Pennsylvania State University, University Park, PA 16802, USA

¹¹ Department of Physics and Astronomy, York University, Toronto, ON M3J 1P3, Canada

¹² Kavli Institute for Astronomy and Astrophysics, Peking University, Beijing 100871, People's Republic of China

¹³ Department of Astronomy, School of Physics, Peking University, Beijing 100871, People's Republic of China

¹⁴ University of Michigan, Ann Arbor, MI 48109, USA

¹⁵ Department of Astronomy, Xiamen University, Xiamen, Fujian 361005, People's Republic of China

Received 2021 May 6; revised 2021 December 22; accepted 2021 December 23; published 2022 February 28

Abstract

We present accretion-disk structure measurements from UV–optical reverberation mapping (RM) observations of a sample of eight quasars at $0.24 < z < 0.85$. Ultraviolet photometry comes from two cycles of Hubble Space Telescope monitoring, accompanied by multiband optical monitoring by the Las Cumbres Observatory network and Liverpool Telescopes. The targets were selected from the Sloan Digital Sky Survey Reverberation Mapping project sample with reliable black hole mass measurements from $H\beta$ RM results. We measure significant lags between the UV and various optical *griz* bands using JAVELIN and CREAM methods. We use the significant lag results from both methods to fit the accretion-disk structure using a Markov Chain Monte Carlo approach. We study the accretion disk as a function of disk normalization, temperature scaling, and efficiency. We find direct evidence for diffuse nebular emission from Balmer and Fe II lines over discrete wavelength ranges. We also find that our best-fit disk color profile is broadly consistent with the Shakura & Sunyaev disk model. We compare our UV–optical lags to the disk sizes inferred from optical–optical lags of the same quasars and find that our results are consistent with these quasars being drawn from a limited high-lag subset of the broader population. Our results are therefore broadly consistent with models that suggest longer disk lags in a subset of quasars, for example, due to a nonzero size of the ionizing corona and/or magnetic heating contributing to the disk response.

Unified Astronomy Thesaurus concepts: [Accretion \(14\)](#); [Quasars \(1319\)](#)

1. Introduction

Although many advances in observing active galactic nuclei (AGNs) have been made, the detailed physics of accretion onto the central engine, the supermassive black hole (SMBH), remains poorly understood. The classic solution for an accretion disk around a compact object is described by Shakura & Sunyaev (1973). The gas infall around a black hole was modeled by a geometrically thin, optically thick accretion disk (hereafter SS73). An effective viscosity causes gas to spiral inwards and converts some of its potential energy into thermal radiation. If the disk is optically thick, the local thermal emission, at least approximately, corresponds to blackbody radiation leading to a continuum emission spectrum, which peaks at ultraviolet (UV) wavelengths in a typical AGN spectral energy distribution.

In the “lamppost” model, the disk is directly illuminated by an extreme-UV and X-ray ionizing source above/below the disk (Galeev et al. 1979; Krolik et al. 1991; Reynolds & Nowak 2003). The ionizing radiation is reprocessed by the disk surface, starting with the inner disk and propagating outward to the outer disk, allowing for coherent continuum variations at different radii (Cackett et al. 2007). The lamppost reprocessing enables the use of correlated interband variability signatures to measure the accretion-disk size and structure from the light-travel time (i.e., τ) between the short- and long-wavelength emission from the disk. This is the basic assumption of the reverberation mapping (RM) technique (Blandford & McKee 1982; Peterson 1993; Peterson et al. 2004) in which physically connected regions “reverberate” in response to the driving continuum. The RM technique has been widely used to estimate the size of the broad-line-emitting region (BLR) and subsequently the SMBH mass from the virial product (Bentz & Katz 2015; usually known as broad-line RM).

Alternatively, the RM technique can be applied to infer accretion-disk size, commonly known as continuum RM. The near-UV and optical continua vary in response to the unobserved far-UV and X-ray ionizing continuum after a time delay.



Original content from this work may be used under the terms of the [Creative Commons Attribution 4.0 licence](#). Any further distribution of this work must maintain attribution to the author(s) and the title of the work, journal citation and DOI.

Table 1
Quasar Sample Information

RMID	R.A. deg	Decl. deg	z	i mag	Var ^a %	$\log \lambda L_{3000}$ (erg s ⁻¹)	$\log M_{\text{BH}}^{\text{a}}$ (M_{\odot})	$\log(L/L_{\text{Edd}})$	SS73 τ_0^{c} days
267	212.80299	53.75199	0.588	19.6	19.4	44.41	7.42 ^{+0.17} _{-0.17}	-0.39	0.31
300	214.92128	53.61379	0.646	19.5	18.2	44.87	7.6 ^{+0.17} _{-0.20}	-0.12	0.51
399	212.63053	52.25938	0.608	20.1	23.6	44.22	7.91 ^{+0.16} _{-0.20}	-1.09	0.39
551	212.94610	51.93883	0.681	21.5	10.3	44.33	6.95 ^{+0.19} _{-0.19}	-0.01	0.2
622	212.81328	51.86916	0.572	19.6	17.2	44.50	7.94 ^{+0.19} _{-0.16}	-0.83	0.5
634	212.89953	51.83459	0.651	20.8	13.2	44.06	7.56 ^{+0.26} _{-0.24}	-0.88	0.26
824	212.65879	52.00913	0.846	21.5	36.6	44.20	8.63 ^{+0.45} _{-0.45}	-1.82	0.67
840	214.18813	54.42799	0.244	18.6	50.0	43.49	7.93 ^{+0.21} _{-0.20}	-1.83	0.22

Notes.

^a The fractional variability is the ratio of the rms to the average maximum likelihood flux calculated using the PrepSpec (Shen et al. 2016) software. The values reported here are computed from the existing 2014–2017 SDSS-RM PrepSpec lightcurves (<http://star-www.st-and.ac.uk/~kdh1/pub/sdss/2017b/sdss.html>), as reported in Shen et al. (2019) for the first-year SDSS-RM data.

^b The black hole masses are drawn from Grier et al. (2017).

^c The expected SS73 disk-size priors as computed from Equation (7) (see Section 5.1).

Continuum RM enables studies of accretion-disk structure by measuring the time delay of causally connected regions of the accretion disk. The continuum RM technique has proved to be more challenging compared to broad-line RM. This is largely because accretion disks are smaller than the BLR, so continuum lags are typically much smaller than broad-line lags. Nevertheless, continuum RM is the most promising technique to learn about SMBH accretion physics for quasars in the distant universe.

Early continuum RM studies established the stratified temperature profile of accretion disks, showing cooler material at larger radii (Krolik et al. 1991; Wanders et al. 1997; Collier et al. 1998, 2001). Several recent monitoring campaigns have been dedicated to accretion-disk studies using continuum RM in nearby AGNs (Sergeev et al. 2005; McHardy et al. 2014; Shappee et al. 2014; Edelson et al. 2015; Fausnaugh et al. 2016; Edelson et al. 2017; Fausnaugh et al. 2018; McHardy et al. 2018). The results indicate a strong correlation of lightcurve variability in the UV–optical with UV variations leading those at optical wavelengths. The general trend in disk-temperature profile (i.e., the wavelength scaling) through the continuum emission from inner/hotter to outer/cooler disk regions is consistent with the lamppost model (Cackett et al. 2007) with $\tau \propto \lambda^{4/3}$ as expected by Shakura & Sunyaev (1973).

Most accretion-disk sizes measured from continuum RM are significantly larger than the expectation from the SS73 model. Observations of single, local AGN have reported UV–optical lags that are a factor of ~ 2 – 3 larger than the model expectation (McHardy et al. 2014; Edelson et al. 2015; Fausnaugh et al. 2016; Edelson et al. 2017; McHardy et al. 2018). Similarly, microlensing observations suggest disk sizes that are $\sim 3 \times$ larger than the SS73 disk-size expectation (Morgan et al. 2018). However, multiobject continuum RM measurements of higher redshift (up to $z \approx 1.9$) quasars are mixed (Jiang et al. 2017; Mudd et al. 2018; Homayouni et al. 2019; Yu et al. 2020). Larger than expected UV–optical lags have also been reported for interband optical continuum RM lags from PAN-STARRS (Jiang et al. 2017). Other works on interband optical continuum RM (Mudd et al. 2018; Homayouni et al. 2019; Yu et al. 2020) challenge this common picture, reporting a consistent accretion-disk size with the Shakura & Sunyaev (1973) model; for example, Mudd et al. (2018) and Yu et al. (2020) relax the lag-significance criteria to

compute the disk size directly from the interband optical lightcurves.

The Sloan Digital Sky Survey Reverberation Mapping Project (SDSS-RM; Shen et al. 2015) has been effective in the industrial-scale study of 849 quasars at $z > 0.3$, spanning a diverse quasar population in redshift, mass, and accretion rate (Shen et al. 2019). Recently, Homayouni et al. (2019) used the SDSS-RM survey and Markov Chain Monte Carlo (MCMC) approach to fit the accretion-disk structure and included lag-detection limits to avoid biases in the measured disk sizes; for more discussion, see the Appendix in Homayouni et al. (2019).

The present work describes the results of an intensive, multiwavelength monitoring campaign for eight quasars selected from the SDSS-RM parent sample. We obtained UV monitoring observations from the Hubble Space Telescope (HST) and coordinated ground-based optical monitoring from the Liverpool Telescope and Las Cumbres Observatory. This study includes a diverse sample of quasars in terms of black hole mass (M_{BH}) and accretion rate with UV–optical broadband photometric monitoring beyond the local universe $z > 0.1$. The present work has two primary goals. The first is to measure the UV emission from the accretion disk’s inner regions and compare the differences in the measured disk sizes for a diverse sample of quasars. The second goal is to measure the UV–optical lag to map the stratification of the accretion-disk structure.

In Section 2 we discuss the details of the observations. Section 3 illustrates our custom reduction pipeline. In Section 4 we describe our lag-identification method, lag reliability, and alias removal for each individual target. In Section 5 we present our final UV disk size and accretion-disk model fits and connection to mass and accretion rate. Throughout this work, we adopt a Λ CDM cosmology with $\Omega_{\Lambda} = 0.7$, $\Omega_M = 0.3$, and $H_0 = 70 \text{ km s}^{-1} \text{ Mpc}^{-1}$.

2. Observations

Our set of eight targets for this study is drawn from the 849 quasars of the SDSS-RM sample (see Table 1). These targets are significantly variable with fractional continuum rms variability of 10%–50% measured from the Prepspec software (Shen et al. 2015, 2016) at rest-frame λL_{3000} continuum. These targets probe a broad range of quasar parameter space in redshift, mass, and Eddington ratio. All targets in our sample

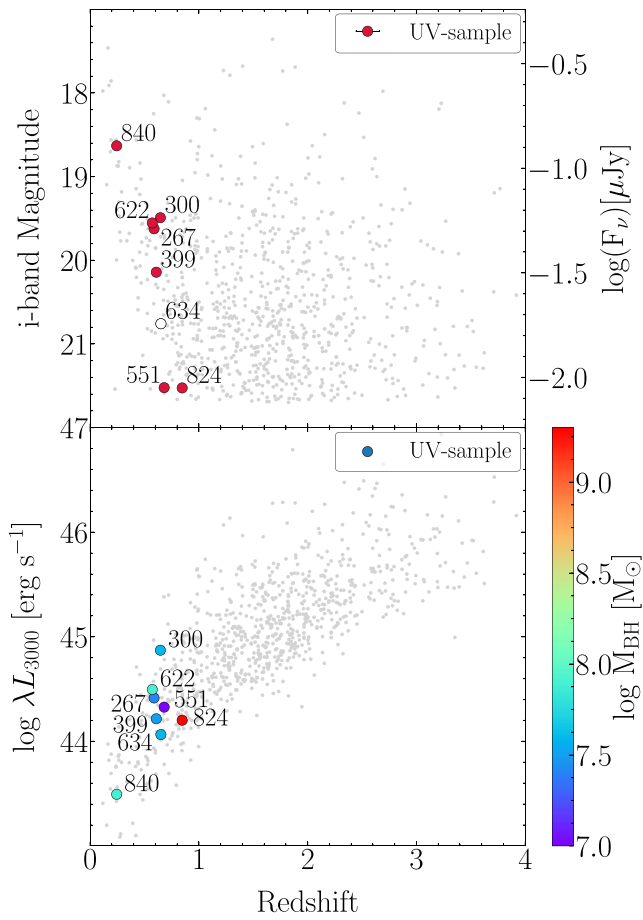


Figure 1. Top: the SDSS-RM parent sample of 849 quasars (gray points) and the set of eight quasars from the UV monitoring campaign (red filled points). The open symbol illustrates RM634, which had a poor signal-to-noise ratio as the result of a DASH observing mode (see Section 3.1). Bottom: our targets probe a wide range of quasar parameter space in λ_{L3000} continuum luminosity and black hole mass, as established for the broader sample in Shen et al. (2019), compared to UV-optical accretion-disk studies for local AGNs.

have RM M_{BH} measurements from the $H\beta$ emission line (Grier et al. 2017), except RM824. We used the single-epoch mass for this particular target, as reported in Shen et al. (2019). Additionally, we selected our targets to have $<10\%$ BLR contamination in the WFC3 F275W filter. This is to minimize the effects of strong emission lines on broadband filters because broad emission lines typically have longer timescales of variability with longer lags and may bias the continuum lightcurves’ underlying shorter lags. Table 1 gives a brief description of our selected sample properties. Figure 1 illustrates the probed quasar parameter space in i -mag, redshift, luminosity, and black hole mass.

2.1. Cycle 25 HST UV Monitoring Campaign

The UV monitoring campaign was executed over two cycles of HST observations (Cycles 25 and 26).¹⁶ Five of the eight quasars (RM399, RM551, RM622, RM634, and RM824) were observed using HST WFC3/UVIS F275W during 2018 March–May over 32 orbits, with an every-other-day cadence and a 63 day duration using four-point dither positions and 64 s

subexposures. These targets were observed using the “Drift-And-Shift,” i.e., the DASH observing design (Momcheva et al. 2017), dropping to gyro guiding after the first target (RM399) to avoid spending time on guide-star acquisition. Due to these targets’ proximity, we fit all five quasars within a single visit. During the DASH sequence, our targets were observed in the following order: RM399, RM824, RM622, RM634, and RM551. Out of the 32 visits, only visit 20 experienced a gyro failure. This visit was later compensated with an additional visit, 33. Furthermore, target acquisition failed in visits 3 and 4, which caused the entire DASH sequence to fail.

The typical drift under HST gyro guiding is $\sim 0''.0015/\text{s}$. However, the last targets (RM634 and RM551) in the DASH sequence often were dropped off the detector. The fourth (RM634) and fifth (RM551) targets were observed at ~ 36 minutes and ~ 45 minutes into each orbit. This indicates a drift $\gtrsim 0''.007/\text{s}$ for RM634 and $\gtrsim 0''.005/\text{s}$ for RM551 that is significantly larger than the expected drift under star guiding. It is possible that our larger drift rate than the mosaic strategy of Momcheva et al. (2017) is caused by the larger slews between pointings while gyro guiding. We conclude that the drift due to dashing is at least 50% of the time $\gtrsim 0''.005/\text{s}$ for our last two targets.

2.2. Cycle 26 HST UV Monitoring Campaign

The UV monitoring campaign observed three other targets (RM267, RM300, and RM840) through HST Cycle 26. These targets were observed during 2019 March–June with WFC3/UVIS F275W using non-DASHed observations over 40 orbits, with an every-other-day cadence and an 80 day duration with 52 s subexposures. All three targets fit in a single visit. However, the available roll angles affected the guide-star availability, which resulted in RM840 being observed for only 33 visits. Removing RM840 from visits 33–40 increased the other two targets’ available exposure time from 52 to 190 s. HST suffered from gyro failure in early 2019, and though it returned to science operations before our monitoring program began, this resulted in longer maneuvering time for target acquisition, which caused failures for two out of the three targets (RM300 and RM840) in visit 22 and failure for all three targets in visit 24.

2.3. Ground-based Monitoring

The HST UV monitoring program was accompanied by coordinated ground-based monitoring from the Liverpool Telescope (LT) and Las Cumbres Observatory Global Telescope Network (LCOGT). The LT observations were performed using the fully autonomous robotic systems with the Spectral imager with a $10' \times 10'$ field of view with a pixel scale $0''.152 \text{ pixel}^{-1}$ (1×1 binning) on the 2 m telescope at the Haleakala site, and the Sinistro imager with a $26' \times 26'$ field of view and pixel scale of $0''.389$ (1×1 binning) on the 1 m telescopes at the McDonald site. The ground-based monitoring design is different between the two cycles of HST monitoring. During Cycle 25, LT/IO:O (infrared–optical:optical) observations provide r -band photometry, while LCOGT provides r -band and z -band photometry. During Cycle 26, we expanded the range of filters and used LT/IO:O to observe in the r and z bands while simultaneously observing in g and i -band with LCOGT. Table 2 provides a short description of each telescope, duration, and number of contributed epochs for this study.

Our ground-based monitoring started before each HST UV monitoring program and extended beyond the completion of

¹⁶ The data can be obtained from the MAST archive at <https://doi.org/10.17909/t9-2cc8-8s52> and <https://doi.org/10.17909/t9-bmkf-m360>.

Table 2
Summary of Observations

Observatory Name	Obs ID	Aperture	Observing Window	Filters	Epochs	Target RMID
HST UV Monitoring						
Hubble Cycle 25	HST 25	DASH	Mar–May (2018)	F275W	32	399, 551, 622, 634, 824
Hubble Cycle 26	HST 26	non-DASH	Mar–Jun (2019)	F275W	40	267, 300, 840 ^a
<i>Ground-based Optical Monitoring</i>						
Las Cumbres (McDonald)	LCOGT	1.0 m	Feb–May (2018)	<i>r</i>	54	551, 622, 824
Las Cumbres (Haleakala)	LCOGT	2.0 m	Feb–May (2018)	<i>z</i>	104	551, 622
Liverpool Telescope	LT	2.0 m	Mar–Jun (2018)	<i>r</i>	80	399, 551, 622, 634, 824
Las Cumbres (McDonald)	LCOGT	1.0 m	Jan–May (2019)	<i>g</i>	57–66	267, 300, 840
Las Cumbres (McDonald)	LCOGT	1.0 m	Jan–May (2019)	<i>i</i>	58–65	267, 300, 840
Liverpool Telescope	LT	2.0 m	Mar–Jun (2019)	<i>r, z</i>	80	267, 300, 840

Note.

^a During Cycle 26, RM840 was observed for 33 orbits due to limited guide-star availability; see Section 2.2.

UV monitoring observations. The extended duration allows the capturing of optical continuum variability, which typically has smaller amplitudes and longer timescales than UV variability. By extending the ground-based monitoring beyond the UV monitoring, we enable detection of longer lags, and high cadence allows detection of short lags. Our ground-based monitoring ideally has a daily cadence. However, the effective cadence due to weather loss was more sparsely sampled (with a mean of ~ 1.5 days).

3. Data Reduction

3.1. HST Cycle 25: DASH Observing Reductions

During Cycle 25, we adopted the “Drift-and-Shift” (DASH) observing method, which reduces the overhead by using unguided, gyro-controlled exposures. This takes advantage of the available time in a single HST visit by removing the requirement for a new guide-star acquisition between pointings. However, due to the lack of guidance sensor corrections, the telescope drift results in an image smeared by $0''.001$ – $0''.002$ per second (Momcheva et al. 2017). The DASH observing method has been successful in other IR wide-field studies such as COSMOS-DASH (Mowla et al. 2019). The WFC3/UVIS and WFC3/IR channels use the same pickoff mirror and Fine Guidance Sensor, and so we would expect both to experience the same telescope drift during gyro guiding, but DASH observing in the UV had not been directly tested until the current study.

Following the DASH observing mode during Cycle 25, we noticed that the smearing effect was far larger than expected in $\gtrsim 90\%$ of visits. The automated reduction from the `astrodrizzle` pipeline (Gonzaga 2012) cannot identify the target from cosmic rays. In particular, the target position shifts across the detector; this shift occasionally changed direction among the four subexposures. The smearing effect varies among the four subexposure dither positions and might extend across several pixels, with the fourth dither position generally being smeared the most. The shifted position of the target in each exposure usually caused it to be removed from the coadded images during cosmic-ray rejection in the standard reductions. We also tested other software for the automated reduction of the cosmic rays such as L.A. Cosmic (van Dokkum 2001). However, we found these methods were only successful for our brightest target (RM622) but failed to identify the rest of the DASHed targets. To perform the photometric UV reductions, we first need to visually inspect to distinguish the target from

the background cosmic rays and then perform the randomly smeared target’s flux measurement.

We used the calibrated, flat-fielded individual exposures (“FLT” files) to locate our targets, visually identifying comparable objects appearing close to each other in successive subexposure images. Our targets are less point like and dimmer than the cosmic rays, resulting in a wider point spread function PSF with a lower maximum, as shown in Figure 2. The average FWHM for RM622 is ~ 2.5 pixels compared to the average cosmic-ray FWHM of 1.3 pixels. This difference also translates to a visual distinction between cosmic rays and targets under extreme pixel distribution scales. Cosmic rays remain white and sharp, whereas our targets become gray and blurry, indicating a more gradual change in flux across the object and lower maximum flux. Additionally, with increased smearing, there is an increased contrast between the cosmic-ray and target PSF and appearance after adjusting the scale, making the most-smearred objects the most conspicuously different among the comic rays.

The first target was always identified because it uses the standard-star guiding. Among the DASH targets, we were only able to locate one of our targets (RM634) in five orbits, and therefore, we discontinued the analysis of this object. The remaining DASH quasars were identified in at least one subexposure image in 82% of the visits.

We used the Astropy `photutils` (Bradley et al. 2017) software package to perform aperture photometry. Identifying the optimum aperture for the flux extraction was complicated by the DASH observing method because the targets blurred into different shapes in each subexposure dither pointing. To account for this, we performed aperture photometry with circular apertures of increasing radii, r_{aperture} . We adopted the circular aperture after comparing the signal-to-noise ratio (S/N) from circular, rectangular, and elliptical apertures for different exposures (see the discussion below). Testing the radii on a range of $0 < r_{\text{aperture}} < 10$ pixels was sufficient for most targets but this was adjusted for more-smearred targets to a range of $0 < r_{\text{aperture}} < 20$ pixels. We estimated the local background within a circular annulus of r_{inner} to be equal to the maximum of the range for r_{aperture} and $r_{\text{outer}} = r_{\text{inner}} + 2$ pixels. This results in an aperture mask for each subexposure dither pointing. We use the sigma-clipped median estimator to obtain the local background. Using a median avoids outliers caused by the presence of high-flux cosmic rays in the annulus. The total background within each aperture is the local background times the circular aperture area.

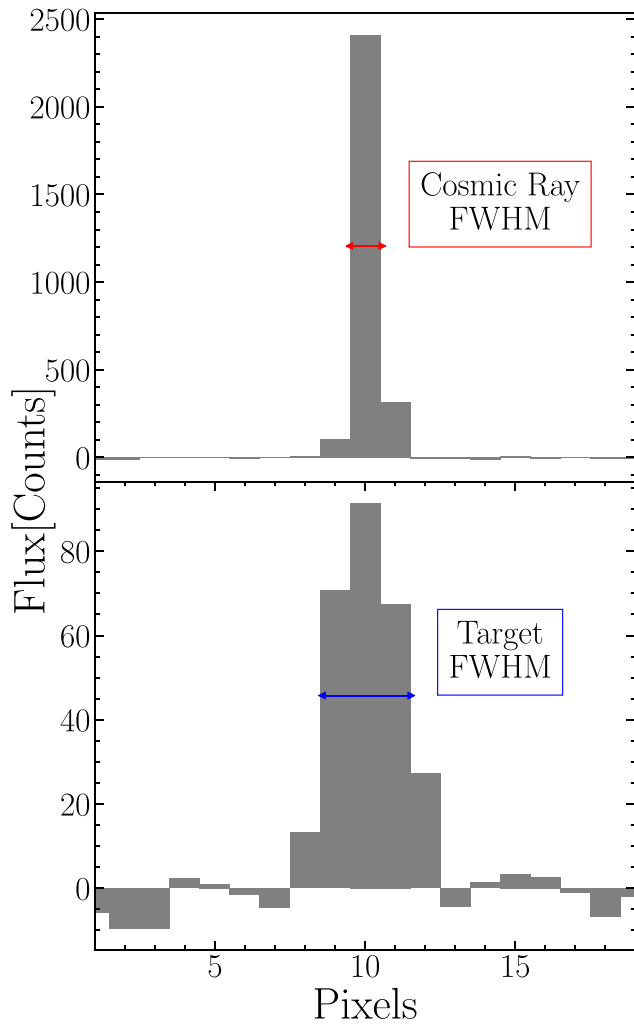


Figure 2. Comparison between the FWHM for a cosmic ray and FWHM of the target: RM622. Cosmic rays typically appear with sharp edges on the image and thus have a narrower FWHM compared to a point-source quasar. We used this additional identification method during the visual inspection to distinguish our quasar targets from cosmic rays.

We chose the aperture size to include 90% of the object flux, illustrated in Figure 3. We performed this analysis on each subexposure dither pointing while visually inspecting each image.

We were able to obtain photometry from 70% of the subexposure images. Photometry failed for targets that overlapped with cosmic rays and/or were too smeared or drifted off the detector (see Section 2.1).

In some exposures, the target and a cosmic ray overlapped, making the individual flux from each indistinguishable. This contamination is observed as a large, steep jump in the smoothly increasing target flux where the relatively high-flux, point-like cosmic ray is incorporated. Additionally, targets were sometimes excessively smeared and blended too much with the background (usually with $r_{\text{aperture}} > 15$ pixels). This level of smearing resulted in inaccurate and outlying low-flux measurements for a visit. For these targets, we tested rectangular and ellipse apertures. However, we found these exposures have a much smaller S/N than the median target flux, and thus we rejected those subexposure dither pointings. Our method of examining the flux for a range of radii across the

target allowed for clear identification and rejection of targets subject to both of these issues.

We compute UV flux uncertainties assuming a Poisson error distribution. We use the error array of the flat-fielded final pipeline outputs (FLTs) and compute the total flux uncertainty in each subexposure, σ_{tot} , by adding the measurement uncertainties inside each aperture in quadrature, such that the $\sigma_{\text{tot}}^2 = \sum_{\text{aperture}} \sigma_{\text{error}}^2$.

We use the reduced UV flux and flux-uncertainty measurements to compute the relative continuum UV lightcurve for four quasars (excluding RM634). We improved the final lightcurve quality by rejecting outlier flux measurements that were offset by more than three times the normalized median absolute deviation (NMAD; e.g., Maronna et al. 2006). This excludes measurements affected by cosmic rays and/or large smearing.

3.2. HST Cycle26: UV Monitoring Reductions

For Cycle 26, we follow a similar reduction protocol as Cycle 25. Even though these observations are not performed using the DASH method, we adopt the Cycle 25 custom reduction approach to remain consistent between our two sets of HST observations. We use the flat-fielded subexposures at each dither positions and perform aperture photometry using the Astropy `photutils` (Bradley et al. 2017) software package. We test a sequence of 50 circular apertures in the range $1 < r_{\text{aperture}} < 15$ pixels while estimating the local background from the sigma-clipped median estimator (see Section 3.1). We obtain the optimal aperture by computing the local maxima in the sum of flux over each r_{aperture} . We compute the final target flux as 90% of the maximum flux, computed from the sum of pixels in the optimal aperture from the background-subtracted, flat-fielded image. We estimate the flux uncertainties using the sum of error squares by placing the optimum aperture over the flat-fielded direct error outputs. We use these final fluxes and uncertainties to produce the relative photometric lightcurve for the three targets observed during Cycle 26.

After the custom reduction of the subexposure images was complete, we remove any bad measurements or outliers from the lightcurves. Some of the subexposures during Cycle 26 were affected by a persistent HST gyro issue that caused the telescope to take much longer to acquire guide stars in between pointings. When this occurred, the telescope continued guide-star acquisition through a significant portion (up to 30 s) of the first exposure of the sequence. This affected five out of 160 subexposures for RM267, 17 out of 160 subexposures for RM300, and 17 out of 132 subexposures for RM840. We removed these flagged subexposures from our final lightcurves. Similar to Cycle 25, we also excluded all subexposures that were offset by $> 3\text{NMAD}$ from the median lightcurve.

3.3. Optical Monitoring Relative Photometry

To produce the relative photometric lightcurves for the ground-based observations, we select five standard stars for each telescope/field/pointing. We perform aperture photometry using the `photutils` (Bradley et al. 2017) software package on the five standard stars of a magnitude similar to that of the quasars. Stars of similar brightness and color (compared to the target quasar) help in identifying atmospheric effects distributed across the field of view for a uniformly selected

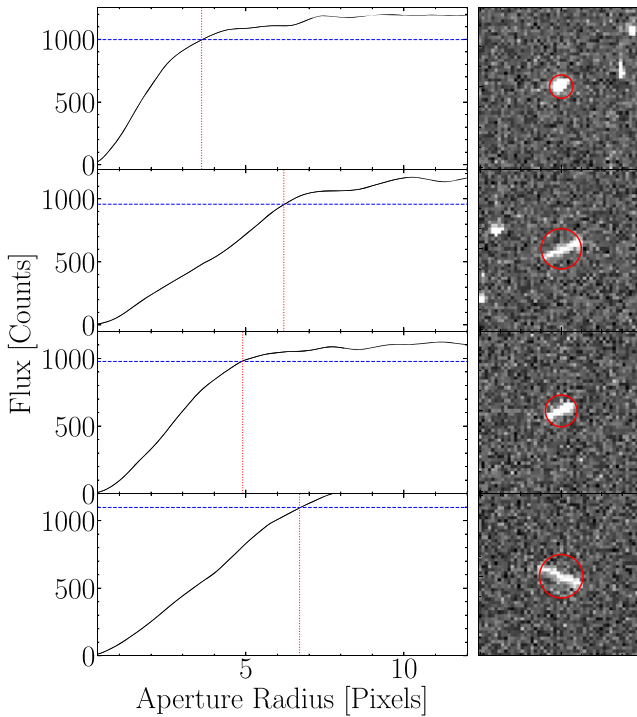


Figure 3. Right: an example of the four subexposure images for one of the quasars (RM622) observed with the DASH method. The target smearing varies in shape and direction, resulting in maximal smearing in the fourth image in this example. Left: curves of growth for the flux as a function of aperture radius. We performed aperture photometry on a sequence of increasing circular radii ranging from 0 to 12 pixels. The chosen aperture size corresponds to 90% of the target’s flux saturation point (blue horizontal dashed line). The red vertical dotted line illustrates the final radius in pixels.

sample of reference stars and to avoid detector saturation (for bright references) and low S/Ns (for faint references). Ideally, one is encouraged to utilize more references stars, however, here we chose five reference stars to remain consistent among all of our fields based on the availability of references. We extract the relative flux by calculating the ratio of the quasars’ net integrated counts, F_{qso} to the sum of all the comparison stars, F_{*} :

$$F_{\text{rel}} = \frac{F_{\text{qso}}}{\sum_i^n F_{*i}}, \quad (1)$$

where the i index indicates the ensemble’s standard star. The aperture photometry is performed similarly to Sections 3.1 and 3.2, computing the rate of flux increase in the flat-fielded, sky-background-subtracted image over 100 circular apertures in the range $1 < r_{\text{aperture}} < 20$. We estimated the local sky background for each target from $r_{\text{inner}} = r_{\text{aperture}} + 3$ pixels to $r_{\text{outer}} = r_{\text{aperture}} + 6$ pixels. We find the optimal aperture for each quasar per observation using the local maxima of the flux increase over the aperture sequence. We extract the relative star lightcurves and, after visual inspection, substitute any variable star lightcurve with non-variable replacements.

We compute the flux uncertainties assuming Poissonian error for each aperture. We propagate the uncertainties from all apertures to derive the error in relative flux measurements. First, the uncertainty from each aperture photometry measurement of each standard star is combined in quadrature to give

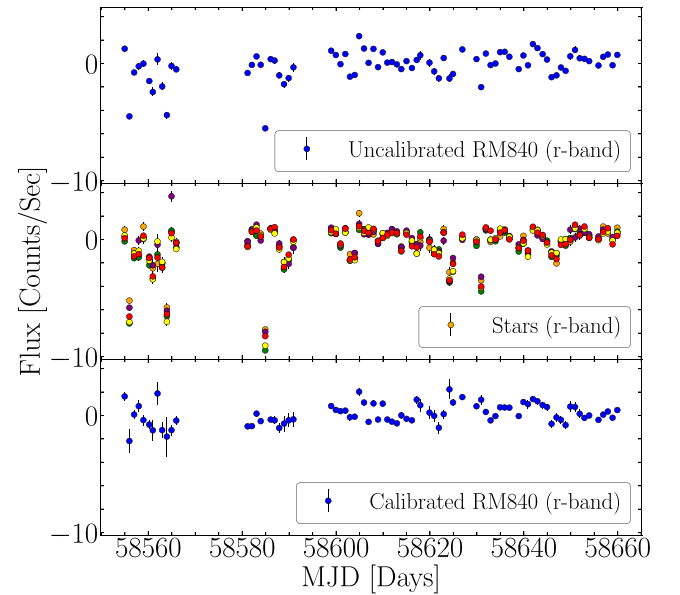


Figure 4. Uncalibrated r -band lightcurves for the quasar RM840 (top) and a standard star in the same images (middle), and the final r -band relative flux lightcurve for the quasar (bottom). For each quasar we select five standard stars to control for weather and instrumental effects on the raw, uncalibrated lightcurves and produce calibrated relative photometry of quasar variability (see Section 3.3). After we produce the relative flux lightcurve, any outlier epochs that are offset by $>3 \times \text{NMAD}$ are rejected from the final lightcurve. For clarity, each of the reference stars and quasar lightcurves is displayed with a mean of zero, and error bars are normalized to NMAD of 1.

the total star ensemble uncertainty:

$$\sigma_{* \text{ ensemble}} = \sqrt{\sum_i^n \sigma_{*i}^2}, \quad (2)$$

where σ_{*} is the uncertainty of each star in the ensemble, and index i is the number of standard stars. The propagated relative flux uncertainty is then given by

$$\sigma_{\text{rel}} = \frac{F_{\text{qso}}}{F_{* \text{ ensemble}}} \sqrt{\frac{\sigma_{\text{qso}}^2}{F_{\text{qso}}^2} + \frac{\sigma_{* \text{ ensemble}}^2}{F_{* \text{ ensemble}}^2}}, \quad (3)$$

where F_{qso} is the net integrated counts per second in the quasar aperture, F_{*} is the sum of the net integrated counts per second in the ensemble of standard stars, σ_{qso} is the uncertainty in the quasar aperture, and $\sigma_{* \text{ ensemble}}$ is the uncertainty of the standard-star ensemble from Equation (2). We compute the relative flux and flux uncertainties from Equations (1) and (3) respectively, using individual apertures for each standard star, quasar, filter, and field to produce all ground-based lightcurves. See Figure 4 for an example of this comparison between the raw and relative lightcurve. We also experimented with other photometric extraction techniques, including difference imaging as implemented by Danida (Bramich 2008) but this led to similar S/N. We test the impact of the optical lightcurve S/N on the measured lags in the Appendix.

We used the weighted average between repeated exposures within a night and computed the final lightcurves. We additionally removed any measurements that were offset by $3 \times \text{NMAD}$ from the median of the entire lightcurve.

An examination of the lightcurve variability between epochs reveals that custom relative photometry reduction may

introduce overestimated errors that mask the underlying flux variability. We follow the procedure outlined in Grier et al. (2017), Grier et al. (2019), and Homayouni et al. (2020), and apply error rescaling by using the lightcurve intercalibration step described below.

4. Time-series Analysis

4.1. Lightcurve Intercalibration

Supplementary ground-based optical monitoring with LCOGT and LT observations provide sufficient cadence to generate well-sampled lightcurves over multiple bands (g , r , i , z). To perform the lag analysis, we must merge observations from different telescope sites with different seeing, filter throughputs, and local sky backgrounds on the same flux scale by intercalibrating each target’s lightcurve.

We perform this intercalibration by using the CREAM (Continuum REprocessing AGN MCMC; Starkey et al. 2016, 2017) merging feature to combine lightcurves at the same wavelength but taken from different telescopes. CREAM uses an MCMC approach to fit a normalized driving lampost model to continuum lightcurve and the accretion-disk response function, and infer the posterior probability distribution for the disk temperature T_1 , temperature slope α , and disk inclination i (Starkey et al. 2016). During this process, CREAM performs the merging by transforming the old lightcurve $f_{j,\text{old}}(\lambda, t)$ to the new lightcurve using $f_{j,\text{new}}(\lambda, t)$ following Equation (3) in Grier et al. (2017),

$$f_{j,\text{new}}(\lambda, t) = (f_{j,\text{old}}(\lambda, t) - \bar{F}_j) \frac{\Delta F_{\text{REF}}}{\Delta F_j} + \bar{F}_{\text{REF}}, \quad (4)$$

where \bar{F}_j and ΔF_j are the mean and standard deviation of the j lightcurve respectively, which will be mapped onto the reference lightcurve with mean and standard deviation \bar{F}_{REF} and ΔF_{REF} using Equation (4); also, CREAM can adjust the underestimated (or overestimated) error bars by adding two parameters to model inaccurate error bars. For each telescope/filter lightcurve, the rescaled lightcurve is computed using

$$\sigma_{ij}^2 = (S_j \sigma_{\text{old},ij})^2 + V_j, \quad (5)$$

where i indicates the number of data points for each telescope/reference lightcurve, V_j is the extra variance, and S_j is the scale-factor parameter. The likelihood function for each telescope/filter lightcurve penalizes large values of V_j and S_j .

CREAM simultaneously fits the offset and rescaling parameters we use to intercalibrate observations from different sites and rescales the overestimated lightcurve uncertainties while also inferring the lampost lightcurve that drives the continuum variability. This paper’s entire time-series analysis is performed using the rescaled and intercalibrated lightcurves generated from CREAM.

4.2. Lag Identification

We adopt two time-series analysis methods for measuring reverberation lags: JAVELIN (Zu et al. 2011) and CREAM (Starkey et al. 2016, also see Section 4.1). Similar to CREAM, JAVELIN (Zu et al. 2011) uses a damped random walk (DRW) model to describe the stochastic variability of the quasar lightcurves. Even though the DRW model may be an incomplete description for quasars on short timescales (Mushotzky et al. 2011; Kozłowski 2016), studies have shown that the DRW model

still provides a flexible approach to accurately measuring lags (Li et al. 2019; Read et al. 2020) and a reasonable fit to observations of quasar variability on the timescales of our monitoring program (days to weeks) (Kelly et al. 2009; MacLeod et al. 2010, 2012; Kozłowski 2016).

JAVELIN uses an MCMC approach using a maximum likelihood method to fit a DRW model to the UV and optical continuum lightcurves, assuming that the local accretion-disk response is a top-hat function and the reverberating lightcurve model is the smoothed, scaled, and shifted version of the UV continuum lightcurve.

We allow the DRW amplitude to be a free parameter but fix the DRW damping timescale to 100 days. Our campaign duration (~ 80 days) is much smaller than the typical damping timescale of a quasar (~ 1500 days in the observed frame; see Kelly et al. 2009; MacLeod et al. 2012). Thus, the damping timescale’s exact value does not matter, so long as it is longer than the campaign’s duration (the lightcurves are effectively modeled as a red-noise random walk with minimal damping). We also tested damping timescales of 200 and 300 days and found no significant differences in the measured lags, as also investigated by Yu et al. (2020).

The optical lightcurve response is parameterized as a top-hat transfer function, assuming a lag and scale factor with a free parameter. The top-hat transfer function in JAVELIN is a simplification of the actual transfer function from the accretion disk, which may be extended with a long tail at large lags and affect the JAVELIN measurements (Starkey et al. 2016). This means that the JAVELIN measurements may be underestimates of the actual mean disk lags. However, the top-hat transfer function is commonly adopted in other works (Jiang et al. 2017; Homayouni et al. 2019; Yu et al. 2020) and so we adopt the simple top-hat transfer function here to provide consistency for comparison of our lag measurements with previous work. We fix the transfer-function width to be 0.5 days, which is sufficiently short compared to the expected lag ($1 < \tau < 14$ days). We tested a wide range of transfer-function widths of 0.1–10 days, which affected the convergence of the MCMC chain in JAVELIN but did not significantly affect the best-fit lag (so long as the JAVELIN chain still converged). We adopt a lag search range of ± 45 days (Cycle 25) and ± 60 days (Cycle 26), chosen to be $\sim 2/3 \times$ of the ~ 60 and ~ 80 days monitoring duration. All of our final measured lags (see Table 4) are significantly shorter than these search ranges. JAVELIN returns a lag-posterior distribution from 62500 MCMC simulations, which are used to compute JAVELIN lag, τ_{jav} , and its uncertainty. Among the targets in our sample, JAVELIN was unable to obtain a continuum model for RM551 using the final CREAM-rescaled error bars and successfully produced the DRW lightcurves only after we further rescaled the error bars by $\sim 80\%$ (see Figure set for RM551).

We also use the CREAM Python wrapper, PyceCREAM¹⁷ to infer accretion-disk lags in addition to the intercalibrating lightcurves (see Section 4.1). We probe lags of ± 50 days to obtain CREAM lag-posterior distributions.

The JAVELIN/CREAM MCMC posterior-lag distributions may have a few ancillary peaks that accompany a primary peak. To identify the reverberating lag from lag-posterior distributions, we smooth each posterior by a Gaussian filter

¹⁷ <https://github.com/dstarkey23/pycecream>

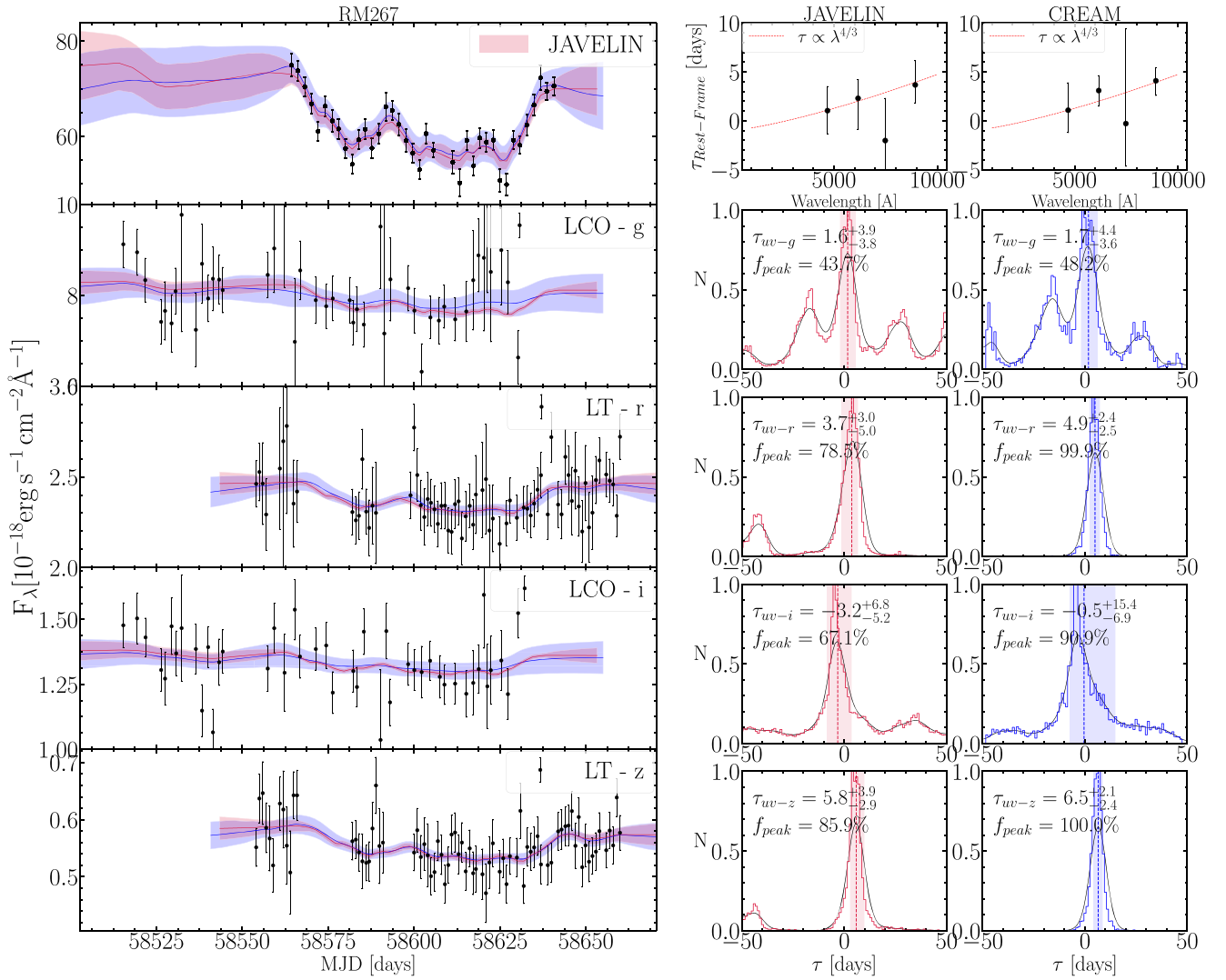


Figure 5. Left: continuum F275W lightcurve (top) and the optical *griz* lightcurves are shown, respectively, from top to bottom for RM267. For each lightcurve, the best-fit DRW model and uncertainty are displayed in the shaded region for JAVELIN (red) and CREAM (blue). The F275W lightcurves displayed here show the weighted-average observations for the four-point dither positions. Top Right: the rest-frame lags (with respect to the UV) vs. optical wavelength, with a $\tau \propto \lambda^{4/3}$ relation shown as a red line. The bottom panels show the UV-optical lag-posterior distribution for JAVELIN (left/red) and CREAM (right/blue) and the final observed-frame lag is displayed for each method. For each lag-posterior distribution, the final observed-frame lag and the 16th/84th percentile error bar are illustrated by the vertical dashed line and the shaded region, respectively. The complete figure set (7 images) is available for all targets.

with a 3 day σ (the width of the smoothing was determined by visual inspection). We then identify the primary peak of the posterior distribution from the peak with the largest area and treat the smaller-area peaks as insignificant lags. The final lag, τ , and the lag 1σ uncertainty is computed from the median, and the 16th and the 84th percentiles of the posteriors in the primary peak.

For each target, we measure the interband lags between the F275 W filter, $\lambda_{\text{pivot, uv}} = 2704 \text{ \AA}$, and optical *g*, *r*, *i*, and *z* bands at $\lambda_{\text{cent}} = 4686, 6166, 7480, \text{ and } 8932 \text{ \AA}$, respectively. Figure 5 (see also the complete figure set related to Figure 5) illustrates each target’s UV and optical lightcurve, JAVELIN and CREAM lag-posterior distributions, and the rest-frame lag compared to SS73 wavelength scaling. In this work, we use both methods to perform the accretion-disk analysis. This enables comparison of both methods’ lag results considering our medium-quality lightcurves following recent comparisons of lag methodologies for survey-quality RM observations (Li et al. 2019) and continuum RM accretion-disk lag methods

(Chan et al. 2020) and their implications for a statistical approach to modeling the disk structure.

Using either method, we find that the JAVELIN and CREAM lags generally produce consistent lag posteriors. There are three lag posteriors where the final lags are inconsistent; UV – *z* in RM551 and UV – *r* and UV – *z* in RM622 (see the figure set). In all these cases, JAVELIN detects a larger negative lag compared to CREAM. This may be due to larger lightcurve uncertainties where JAVELIN is originally unable to fit a DRW without any custom error bar rescaling (see the discussion earlier in this section). It also might indicate that a top hat is an oversimplified assumption for the disk-response function in this quasar. CREAM uses a disk-response function that rises rapidly to a peak and has a long tail toward large lags and is likely a better description of the disk response.

We find that in most cases the longer wavelength continuum variation lags behind those at shorter wavelengths, as expected for reverberation in a lamppost model. However, the increasing lag with wavelength has exceptions in the *i*-band filter. For

Table 3
BLR Contamination

RMID	Emission-line Contamination (%)			
	<i>g</i> band	<i>r</i> band	<i>i</i> band	<i>z</i> band
RM267	0.7	...	4.3	...
RM300	0.1	...	0.5	...
RM399	0.8	...	2.4	...
RM551	0.2	...	7.4	...
RM622	0.7	...	3.6	...
RM634	0.2	...	0.5	...
RM824	1.5	6.8
RM840	...	1.8	13.0	...

targets where we have multiband observations, we see that *i*-band observed-frame lag is occasionally much shorter, $\tau = -3.2^{+6.8}_{-5.2}$ days (RM267; see Figure 5), or much longer, $\tau = 23.4^{+6.6}_{-7.8}$ days and $\tau = 35.6^{+5.9}_{-5.1}$ days (RM300 and RM840, respectively) than lags in other filters. In addition, the *g*-band lag for RM840 is much larger than expected, $\tau = 32.1^{+5.7}_{-4.9}$ days (see figure set). These larger lags could be due to effects from the emission lines in the BLR, contributions from the iron pseudo-continuum or the diffuse Balmer continuum (Korista & Goad 2001; Lawther et al. 2018; Korista & Goad 2019). We will discuss these contributing factors and other lag-measurement reliability components in Section 4.3. It is more difficult to assess the trend of larger lags at longer wavelengths for those targets that were observed as part of Cycle 25 due to lag aliasing issues and larger uncertainties. That said, we find that the CREAM lags in RM551 are in agreement with a larger lag at longer wavelengths.

4.3. BLR Contamination

One plausible scenario for longer continuum lags is that these lags may be originating in the BLR, where the BLR or diffuse emission significantly contributes to the variability measured in the photometric filter, and the typically longer BLR lags make the measured photometric lag larger than expected solely from continuum lags.

Some investigation of these larger lags reports that the BLR emission is responsible. Fausnaugh et al. (2016) and Cackett et al. (2018) found evidence for nebular BLR contamination in specific filters, and Chelouche & Zucker (2013); Chelouche (2013) found this to be a widespread phenomenon. Considering the wavelength range of our observations and our target redshifts, we investigated the effect of BLR contamination from prominent BLR emission lines: Ly α λ 1215, C IV λ 1549, C III] λ 1909, Mg II λ 2800, He II λ 4687, H β λ 4861, and H α λ 6563. To compute the BLR contribution, we examine whether an emission line falls in the filter bounds in the quasar’s observed frame. If so, we then use the ratio of emission-line equivalent width, $EW_{\text{line, rms}}$ from the Prepspec outputs to the overlapping filter width. Shen et al. (2019) provide a full description of PrepSpec fits applied to first-year SDSS-RM observations.¹⁸ We obtain the fractional BLR contamination by multiplying this ratio by the rms variability of the emission line and nearby continuum (λ 1700, λ 3000, and

λ 5100). Table 3 summarizes the contribution from the BLR emission-line contribution for all objects in our sample. Only the UV – *i* lag in RM840 exhibits a maximum 13% contribution from the H α emission line, which we reject by choosing a BLR contamination rejection threshold of 10%. We note that the H α lag reported for this object (Grier et al. 2017) is only $13.2^{+2.9}_{-3}$ days, which contradicts a simple BLR contamination by H α . The BLR contamination in the rest of our targets falls well below the 10% contamination limit.

In addition to the emission-line BLR contamination, some quasars may have significant contributions from diffuse continuum emission from the BLR clouds (Korista & Goad 2001). The contribution from this variable diffuse emission originates in the BLR, at larger radii than the continuum variability of the accretion disk. Korista & Goad (2001, 2019) have claimed that the diffuse Balmer continuum significantly affects the interband continuum lags observed in NGC7469 (Wanders et al. 1997; Collier et al. 1998; Kriss et al. 2000; Pahari et al. 2020). This effect was particularly apparent near the Balmer jump 3646 Å in the lag spectrum of NGC 4593 (Cackett et al. 2018) and also in other studies of local AGNs (Edelson et al. 2015; Fausnaugh et al. 2016; Edelson et al. 2017, 2019; Cackett et al. 2020). There are two main contributors to the diffuse Balmer continuum. The first source is emission from free-bound transitions (recombination continuum), which affects wavelengths bluer than the Balmer edge. The second contributing factor is blended high-order bound-bound transitions, which results in a diffuse Balmer forest redward of the Balmer edge. This effect could explain the large UV – *g* and UV – *i* lags that are $\gtrsim 10$ days (observed-frame) and overlap with 3646 Å. We thus exclude any observed-frame lags >10 days in filters that overlap with rest-frame λ 3500–3900.

Furthermore, a plethora of weak emission lines from many thousands Fe II transitions in the BLR form a pseudo-continuum that spans UV to near-infrared wavelengths (Vestergaard & Wilkes 2001; Bruhweiler & Verner 2008). This slowly varying Fe II pseudo-continuum introduces uncertainty in the true continuum variability (Kuehn et al. 2008). We thus exclude any outlier lags that overlap the Fe II complex at λ 4434–4684 (Boroson & Green 1992) or λ 5100–5477 (Vanden Berk et al. 2001). The UV Fe II pseudo-continuum at λ 1250–3090 (rest-frame) (Vestergaard & Wilkes 2001) generally has little effect on the continuum fluxes in our observed-frame filters. Typical Fe II equivalent widths are small (<50 Å), and so we anticipate minimal contribution from iron emission. We reject outlier measurements that fall within these windows and have rest-frame lags that are too large (>10 days or <-10 days); the rejected outlier lags include four measurements: $\tau_{\text{uv}-i}(\text{RM300}) = 14.2^{+3.9}_{-4.7}$, $\tau_{\text{uv}-r}(\text{RM399}) = 15.9^{+4.7}_{-4.4}$, $\tau_{\text{uv}-z}(\text{RM551}) = -16.3^{+4.4}_{-4.9}$, and $\tau_{\text{uv}-g}(\text{RM840}) = 25.7^{+4.6}_{-3.9}$ using JAVELIN and $\tau_{\text{uv}-i}(\text{RM300}) = 17.1^{+4.9}_{-5.1}$, $\tau_{\text{uv}-r}(\text{RM399}) = 14.4^{+4.1}_{-3.6}$, $\tau_{\text{uv}-z}(\text{RM551}) = 14.6^{+4.5}_{-4.6}$, and $\tau_{\text{uv}-g}(\text{RM840}) = 25.9^{+3.1}_{-2.7}$ using CREAM. These rejected lags along with other insignificant lags (see Section 4.4 for individual target discussion) are shown with open symbols in Figure 6. The diffuse Balmer and Fe II pseudo-continuum windows are also shown as gray-shaded regions in Figure 7.

4.4. Lag Reliability

The lag-posterior distribution from JAVELIN or CREAM has a primary peak, which corresponds to a flux-weighted mean radius for emission in the bandpass. This primary lag is identified as the smoothed lag-posterior region between local

¹⁸ The PrepSpec outputs from 2014–2017 SDSS-RM observations are available at <http://star-www.st-and.ac.uk/~kdh1/pub/sdss/2017b/sdss.html> (K. Horne et al. 2022, in preparation.)

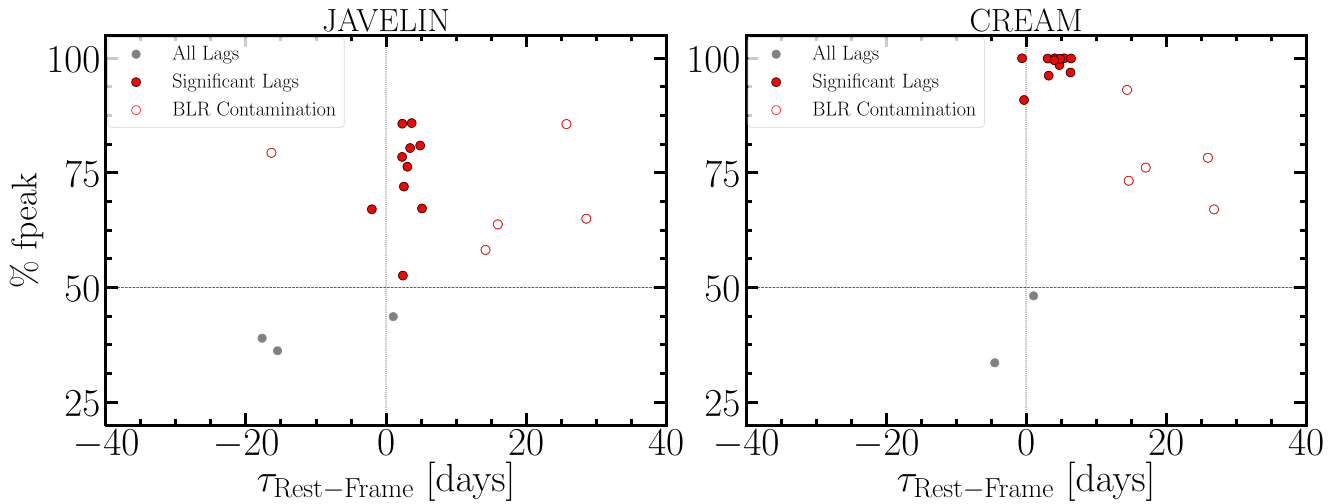


Figure 6. Lag-significance criteria for the JAVELIN (left) and CREAM (right) methods. A lag is significant if its peak (between local minima) includes at least 50% of the lag-posterior samples and has a $<10\%$ contribution from the prominent emission lines. If a prominent broad emission line falls in any of the filter ranges and adds significantly to the continuum variability, the lag is considered contaminated and removed from the significant lag measurements. In addition, the diffuse Balmer continuum at 3646 \AA and the Fe II pseudo-continuum at $\sim 4434\text{--}4684$ and $\sim 5100\text{--}5477$ may contribute to the excess of larger lags in these regions (see Section 4.3). Red open symbols show outlier lags (>10 days or <-10 days in rest frame) that may be affected by diffuse BLR contamination despite having $f_{\text{peak}} > 50\%$.

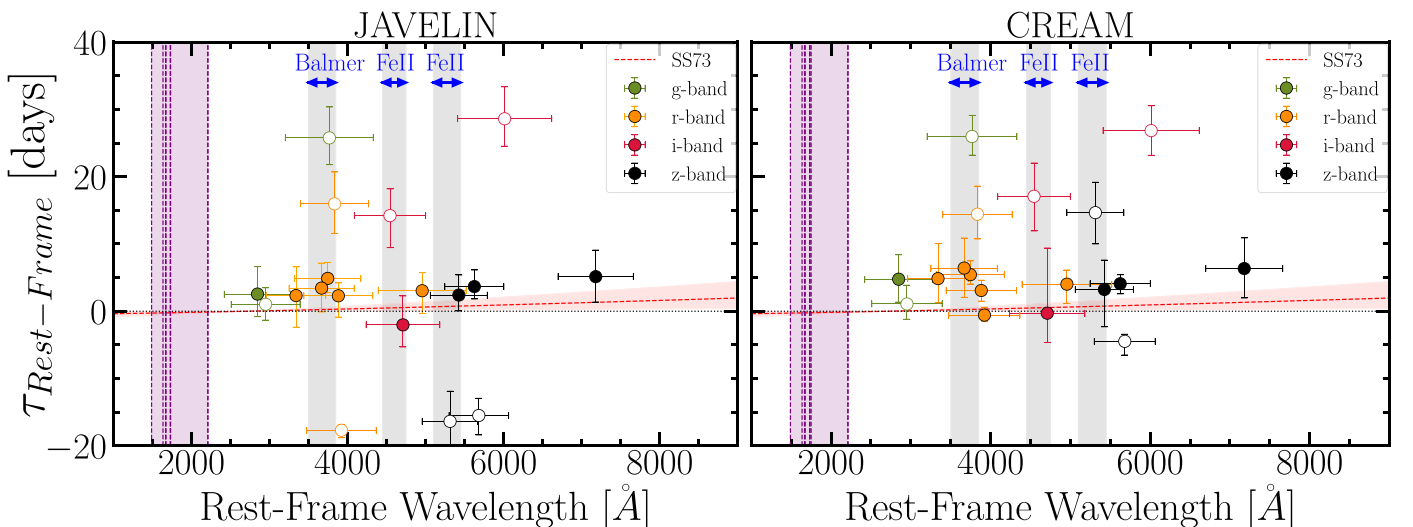


Figure 7. Rest-frame lag as a function of wavelength using JAVELIN (left) and CREAM (right). The colored symbols show the UV $-g$ (green), UV $-r$ (orange), UV $-i$ (red), and UV $-z$ (black). All the lags are computed with respect to the HST UVIS F275W with a normalization wavelength of 2700 \AA . The purple shaded region indicates the range of rest-frame F275W probed by 2750 \AA observed frame, where the purple dashed line corresponds to each quasar in our sample. The red dashed line displays the SS73 model for the mean M_{BH} and mean \dot{M}_{BH} of the sample of significant lags, and the shaded region around the red dashed line illustrates the minimum and maximum SS73 disk size, computed from our sample’s minimum and maximum in M_{BH} and \dot{M}_{BH} . The shaded gray regions illustrate the wavelength regions potentially affected by the Balmer diffuse continuum and the Fe II diffuse continuum. We reject outlier ($|\tau| > 10$ days) lags that overlap with these windows, which results in the rejection of $\tau_{\text{UV}-r}$ in RM300, $\tau_{\text{UV}-r}$ in RM399, $\tau_{\text{UV}-z}$ in RM551, and $\tau_{\text{UV}-g}$ in RM840. We have also rejected $\tau_{\text{UV}-i}$ in RM840 due to high (13%) BLR emission-line contamination from H α . All the rejected lags (see Sections 4.3 and 4.4) are illustrated with open symbols.

minima with the largest area. This primary peak is often accompanied by less-significant peaks, which may be interpreted as alias lag solutions. To ensure that the final reported lags are statistically meaningful, we require “reliable” lags as those containing a minimum of 50% of the lag posterior samples within the primary peak, i.e., $f_{\text{peak}} > 50\%$, following a similar approach to Grier et al. (2017), Homayouni et al. (2019). The f_{peak} requirement ensures a reliable lag solution and removes cases with many alias lags in the posterior.

Figure 6 shows the lag-measurement results for all of the interband lags for our targets. Considering the different

observation designs and optical filter coverage during Cycle 25 and Cycle 26, we cover 18 interband lag measurements. The lag-significance criteria are shown in each panel. Out of the 18 interband lags distributed among 7 targets, JAVELIN finds 10 significant lags and CREAM finds 11 significant lags. Table 4 reports our final significant lag measurements.

We review each target’s lag measurement (for either the JAVELIN/CREAM method). We discuss the lags measured or rejected for each quasar in detail below.

1. *RM267*: For this target, the reliable lag measurements are limited to UV $-r$, UV $-i$, and UV $-z$ lag measurements.

Table 4
Significant Rest-frame UV–Optical Lag Measurements

RMID	Redshift	JAVELIN			CREAM				
		τ_{uv-g} days	τ_{uv-r} days	τ_{uv-i} days	τ_{uv-z} days	τ_{uv-g} days	τ_{uv-r} days	τ_{uv-i} days	τ_{uv-z} days
267	0.588	...	$2.3^{+1.9}_{-3.2}$	$-2.0^{+4.3}_{-3.3}$	$3.7^{+2.5}_{-1.8}$...	$3.2^{+1.5}_{-1.6}$	$-0.3^{+9.7}_{-4.4}$	$4.1^{+1.3}_{-1.5}$
300	0.646	$2.6^{+4.1}_{-3.4}$	$4.9^{+2.4}_{-2.1}$...	$2.4^{+3.0}_{-2.4}$	$4.8^{+3.6}_{-3.4}$	$5.4^{+2.0}_{-1.4}$...	$3.2^{+4.4}_{-5.5}$
399	0.608	-	...	-	-	-	...	-	-
551	0.681	-	$3.5^{+3.7}_{-3.6}$	-	...	-	$6.4^{+4.5}_{-4.4}$	-	...
622	0.572	-	...	-	...	-	$-0.6^{+1.2}_{-1.0}$	-	...
824	0.651	-	$2.3^{+4.3}_{-4.7}$	-	-	-	$4.9^{+5.2}_{-3.6}$	-	-
840	0.244	...	$3.1^{+2.7}_{-3.4}$...	$5.1^{+3.9}_{-3.8}$...	$4.0^{+2.1}_{-2.9}$...	$6.4^{+4.6}_{-4.4}$

Note. We have used two different symbols to distinguish the missing lags. We have identified those lag measurements that did not pass the lag-significance criteria of Section 4.4 with “...” and if the lag measurement was not available because the bandpass was not observed, we have identified it with “-.”

The UV – g lag has $f_{\text{peak}} < 50\%$ and is considered insignificant.

The UV – r lag overlaps with the diffuse Balmer continuum (at $\sim 3882 \text{ \AA}$). However, the rest-frame lag is relatively short, $\tau_{\text{rest-frame (jav)}} = 2.3^{+1.9}_{-3.2}$ days, and therefore it is unlikely to be significantly contaminated by diffuse Balmer emission from the BLR.

- RM300*: For this target, the only reliable lags are UV – g, UV – r, and UV – z lag measurements.

The UV – r lag falls in the diffuse Balmer continuum window at $\sim 3746 \text{ \AA}$. However, the lag is short and so is unlikely to be significantly affected by the diffuse Balmer continuum.

The UV – i lag, on the other hand, overlaps with the Fe II pseudo-continuum at 4544 \AA with rest-frame lag $\tau_{uv-i} = 14.2^{+3.9}_{-4.7}$ days and is therefore rejected from our final reliable lag sample.

The UV – z lag also overlaps with the Fe II pseudo-continuum ($\sim 5426 \text{ \AA}$) but is short ($2.4^{+3.0}_{-2.4}$) and so is consistent with continuum variability dominating the lag rather than diffuse BLR contamination.

- RM399*: The UV – r lag is the only significant lag measurement for this target, and it overlaps with the diffuse Balmer continuum at $\sim 3834 \text{ \AA}$. The size of this lag, $\tau_{uv-r} = 15.9^{+4.7}_{-4.4}$ days, is likely affected by the diffuse Balmer emission. We reject this lag measurement from our final lag sample.
- RM551*: The only reliable lag for this target is the UV – r lag from JAVELIN. The UV – r band at 3668 \AA falls in the diffuse Balmer window; however, the rest-frame lag is too short, $\tau_{uv-r} = 3.5^{+3.7}_{-3.6}$ using JAVELIN and $\tau_{uv-r} = 6.4^{+4.5}_{-4.4}$ using CREAM, to be significantly affected by the diffuse Balmer emission.

The UV – z lag overlaps with the diffuse Fe II pseudo-continuum at 5313 \AA . The reported lag is an outlier from both lag methods (a negative lag using JAVELIN and a large positive lag using CREAM).

- RM622*: The only significant lag for this target is the CREAM UV – r lag. For this target, JAVELIN reports a UV – r lag with $f_{\text{peak}} < 50\%$. But the UV – r lag using CREAM is significant and does not overlap with any diffuse BLR emission windows.

The UV – z lag has $f_{\text{peak}} < 50\%$ using either method and is therefore insignificant.

- RM824*: The UV – r is the only lag measurement for this target and is considered a significant lag with no overlap in the contributing diffuse BLR emission windows.

- RM840*: The UV – r and UV – z lags for this target are considered significant with no contribution from the diffuse BLR windows. The UV – g at rest-frame $\lambda 3766$ lag falls in the diffuse Balmer continuum window. Considering the reported rest-frame lag of $\tau_{uv-g} = 25.7^{+4.6}_{-3.9}$, it is likely that this lag is significantly affected by the diffuse Blamer emission.

The UV – i lag in this target has a significant contribution from the BLR emission line ($H\alpha$) and is therefore rejected from our final lag sample.

Figure 7 illustrates all of our lag measurements, and Table 4 presents a summary of our final significant UV–optical continuum lags for our targets. For the remainder of this analysis, we remove the insignificant lags from our analysis and only use our reliable measurements. We perform accretion-disk structure analysis in Section 5, interpreting the observations in comparison to the SS73 disk expectation.

5. Discussion

One of our UV-monitoring campaign’s main goals is to use the UV–optical time delays to study the inner-disk structure as a function of M_{BH} and accretion rate. Our sample’s redshift range $0.24 < z < 0.85$ translates to wavelength-dependent continuum lags that probe $2847\text{--}7180 \text{ \AA}$ in the quasar rest frame. We note that our significant lags per target include three interband lag measurements at best (see Table 4) as described in detail later in this section, which is not sufficient to constrain accretion-disk parameters for each target individually. We combine the significant lag measurements for our targets (see Table 4) and use a Bayesian approach to fit an accretion-disk model parameterized as

$$\tau_{\text{opt}} - \tau_{\text{uv}} = \tau_0 \left[\left(\frac{\lambda_{\text{opt}}}{2700 \text{ \AA}} \right)^\beta - \left(\frac{\lambda_{\text{uv}}}{2700 \text{ \AA}} \right)^\beta \right] \quad (6)$$

Here τ is the rest-frame lag, λ_{uv} is the rest-frame UV reference wavelength and λ_{opt} corresponds to rest-frame optical wavelengths. In the “standard” optically thick, geometrically thin-disk model (Shakura & Sunyaev 1973), $\beta = 4/3$ and the disk

normalization expectation from SS73 is

$$\tau_{0,SS73} = \frac{1}{c} \left(\frac{45G}{16\pi^6 hc^2} \right)^{1/3} (2700\text{\AA})^{4/3} \chi^{4/3} M_{\text{BH}}^{1/3} \dot{M}_{\text{BH}}^{1/3}. \quad (7)$$

The SS73 disk-size normalization, $\tau_{0,SS73}$, is dependent on the mass of the central black hole, M_{BH} the accretion rate, $\dot{M}_{\text{BH}} = L_{\text{Bol}}/\eta c^2$, where the radiative efficiency $\eta = 0.1$ is assumed and L_{Bol} is the bolometric luminosity. The quantity χ is a geometrical factor accounting for the flux-weighted mean radius and is $\chi = 2.49$. Alternately, a larger value for χ is obtained if the flux is emitted from a single annulus, $\chi = 4.97$ (Kammoun et al. 2021). In this work we use the smaller $\chi = 2.49$ for our main analysis; however, we note that this is one of the theoretical uncertainties of the RM disk interpretation. We adopt the normalization wavelength of 2700 Å based on the UVIS F275W filter pivot wavelength of 2704 Å. We choose a normalization of 2700 Å to make $\lambda_{\text{opt}}^\beta - \lambda_{\text{uv}}^\beta$ in Equation (6) close to unity for the r band (rest-frame) and thus the best-fit τ_0 close to the measured rest-frame lag.

We follow a Bayesian framework to fit a nonlinear model using the software package `PyMC3` (Salvatier et al. 2016) and determine the posterior distribution of accretion-disk parameters described below. We use the SS73 accretion-disk expectations as priors for the MCMC fit. We adopt the likelihood as a Student's T-distribution, which has a heavier tail than a normal distribution and so is more robust to outliers. The Student's T-distribution is centered at the measured lag using either method (JAVELIN or CREAM) with the lag uncertainty. We construct two chains with 20,000 draws, considering only the second half of the chain as post-burn-in draws. We explicitly check for divergences using the Gelman–Rubin statistics (Gelman & Rubin 1992).

5.1. Accretion-disk Size

Our first approach is to use the significant lag measurements from Section 4 and model the disk-size normalization from Equation (6) while fixing $\beta = 4/3$ to match the thin-disk value for the accretion-disk wavelength scaling, i.e., $\langle \tau \rangle \propto \lambda^{4/3}$. We use the SS73 disk normalization for mean M_{BH} , $\langle M_{\text{BH}} \rangle$, and mean accretion rate, $\langle \dot{M}_{\text{BH}} \rangle$, of the quasars with significant lags, following

$$\tau_{0,SS73} = \frac{1}{c} \left(\frac{45G}{16\pi^6 hc^2} \right)^{1/3} (2700\text{\AA})^{4/3} \chi^{4/3} \left(\frac{C_{\text{Bol}}}{\eta c^2} \right)^{1/3} \times \langle M_{\text{BH}} \rangle^{1/3} \langle \lambda L_{3000} \rangle^{1/3}, \quad (8)$$

where $\tau_{0,SS73}$ is the expected value in the SS73 model, and we have assumed $\chi = 2.49$ and $L_{\text{Bol}} = C_{\text{Bol}} \lambda L_{3000}$ with the bolometric luminosity correction of $C_{\text{Bol}} = 5.15$ from Richards et al. (2006). We fit the disk-size normalization by combining Equations (6) and (8):

$$\tau = \tau_0 \left[\left(\frac{\lambda_{\text{opt}}}{2700\text{\AA}} \right)^\beta - \left(\frac{\lambda_{\text{uv}}}{2700\text{\AA}} \right)^\beta \right] \times \left(\frac{M_{\text{BH}}}{\langle M_{\text{BH}} \rangle} \right)^{1/3} \left(\frac{\lambda L_{3000}}{\langle \lambda L_{3000} \rangle} \right)^{1/3} \quad (9)$$

Here we use the monochromatic luminosity λL_{3000} as a proxy for \dot{M}_{BH} and have folded the constants into the disk-size

normalization, τ_0 . In this section, we refer to the best-fit disk-size normalization as τ_0 , whereas the $\tau_{0,SS73}$ describes the SS73 expectation for disk-size normalization. The values for M_{BH} and λL_{3000} are taken from Table 1. Figure 8 shows the result of the single fit and the posterior predictive distribution. We use Equation (8) to compute an accretion-disk normalization prior of 0.5 ± 0.1 days for $\langle \log M_{\text{BH}} \rangle = 7.7 M_\odot$ and $\langle \lambda L_{3000} \rangle = 44.3$ for the JAVELIN significant lags and an accretion-disk size of 0.5 ± 0.1 days for $\langle \log M_{\text{BH}} \rangle = 7.7 M_\odot$ and $\langle \lambda L_{3000} \rangle = 44.4$ for the CREAM significant-lag sample (also see Table 1). We use these values as a prior for the single-parameter fit, $\tau_{0,SS73}$. Using JAVELIN significant lags, we find the best-fit disk normalization from the median of the disk normalization posterior to be $2_{-0.6}^{+0.6}$ days, which is a factor of ~ 4 larger than the mean disk normalization expectation value, and considering the uncertainties, the deviation significance level is $\sim 3\sigma$. Using significant CREAM measurements, we find a slightly larger best-fit value of $3.3_{-0.8}^{+0.8}$ days, approximately 6.5 times larger than the mean SS73 disk-size normalization.

Figure 9 compares our UV–optical lags with the optical–optical continuum lags measured for the same quasars in our previous work (Homayouni et al. 2019). To perform a one-on-one comparison between the UV–optical lags from this study and the earlier optical lag measurements, we translated the UV–optical lag measurements to a disk lag between continuum emission at 2700 Å and 5100 Å using a pivot wavelength of 2700 Å and $\beta = 4/3$ (see Equation (6)). We applied the same conversion to the optical lags of Homayouni et al. (2019) measured between the g and i optical bands. Our UV–optical lags are consistent with the optical lags measured for these targets (excepting one object, not shown in Figure 9, which had a negative optical–optical lag measured by Homayouni et al. (2019)). The observed consistency is further confirmed by our best-fit results for the temperature profile slope, β (see Sections 5.2 and 5.3) because the best-fit $\beta \simeq 4/3$ implies consistent UV–optical and optical–optical lags.

High-cadence UV–optical RM studies of local AGNs have frequently reported larger disk sizes than the standard thin-disk prediction (Edelson et al. 2015; Fausnaugh et al. 2016; Cackett et al. 2018; McHardy et al. 2018; Edelson et al. 2019). These studies report average lags that are larger by a factor of ≈ 3 –4 than SS73 predictions even after accounting for diffuse BLR contamination affecting the U -band wavelengths (see Section 4.3). On the other hand, “industrial-scale” photometric monitoring projects with larger and more diverse samples of quasars show average disk lags that are consistent with the SS73 model, but with significant scatter about the mean (Mudd et al. 2018; Homayouni et al. 2019; Yu et al. 2020).

At first glance, our large continuum lags agree with the previous work on nearby AGNs with disk sizes larger than the SS73 expectation. But it turns out that the quasars of this work represent only a limited subset of the larger SDSS-RM sample in terms of their measured disk sizes. The UV–optical lags are consistent with the optical–optical lags of the same quasars, as shown in Figure 9, and so our measurements are consistent with a small sample that is preferentially drawn from the high side of the large scatter in disk lags among the broader quasar population. In other words, our small sample of UV–optical targets is consistent with being biased to only the high-lag portion of the broader range of quasar disk sizes. There is no obvious bias in our HST sample selection that would prefer

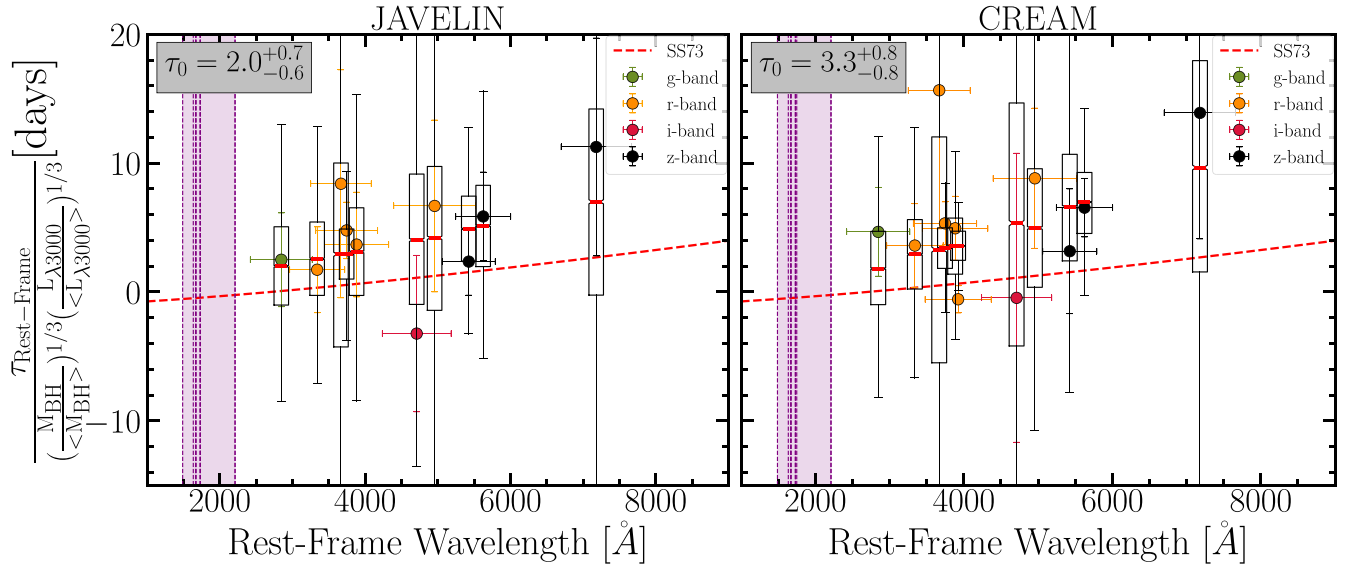


Figure 8. Rest-frame lags normalized by the ratio of M_{BH} and λL_{3000} vs. wavelength using JAVELIN (left) and CREAM (right). Here we show the best-fit result (see Section 5.1) from a simple accretion-disk model where the only free parameter is the disk normalization, τ_0 (see Equations (6) with fixed $\beta = 4/3$). The colored points are the interband accretion-disk significant lags (same as Figure 7). The box plots illustrate the 25th and 75th percentiles of the posterior predictive distribution, and the thick red line marks the median of the posterior predictive distribution at each lag measurement (filled circles). The extended whiskers show the 5th to 95th percentiles of the posterior predictive distribution. For the majority of our lag measurements, the model is a good representation of the data with the lag measurements overlapping within the 25th and 75th percentiles of the posterior predictive distribution.

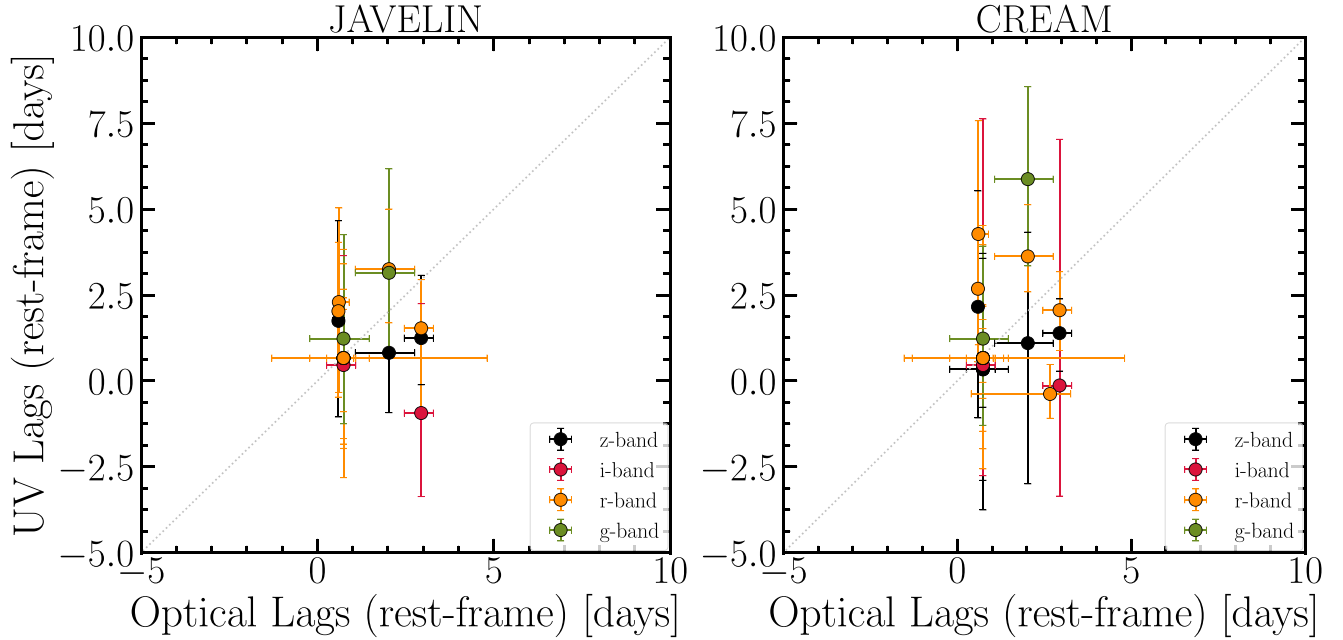


Figure 9. Rest-frame UV-optical lags vs. optical lags measured from Homayouni et al. (2019) using JAVELIN (left) and CREAM (right). For this comparison, we have converted the UV-optical from the current study as well as the optical g and i lags from Homayouni et al. (2019) to a common disk size, where this common disk size corresponds to the relative distance differences between 2700 \AA and 5100 \AA . On average our UV-optical lags are in agreement with each other. Colored points correspond to each UV-optical lag. The gray dotted line shows the 1:1 ratio.

long UV-optical disk lags, and so we instead assume that this is simply a random result of selecting a small sample.

There are several possible explanations for disk lags being larger than the SS73 expectation in some subsets of quasars. Chelouche (2013) argues that contribution from widespread diffuse nebular emission can increase measured continuum lags. We find evidence for this effect by diffuse nebular and iron emission, but only in specific wavelength regions, and so our work does not support the idea that diffuse nebular emission has a widespread effect on continuum lags at all

wavelengths. A different reprocessing geometry, i.e., a larger χ factor in Equation (7), might also lead to larger continuum lags. Kammoun et al. (2021) consider the reprocessing of emission from a point-source, lamppost corona by a Novikov-Thorne general relativistic disk, including the effects of disk ionization and a potentially large height of the corona above the disk, and obtain results consistent with a larger χ factor. Their results also do not rule out an extended corona. More complicated disk reprocessing, like the magnetic-coupling model of Sun et al. (2020), would also increase the measured lag in some quasars.

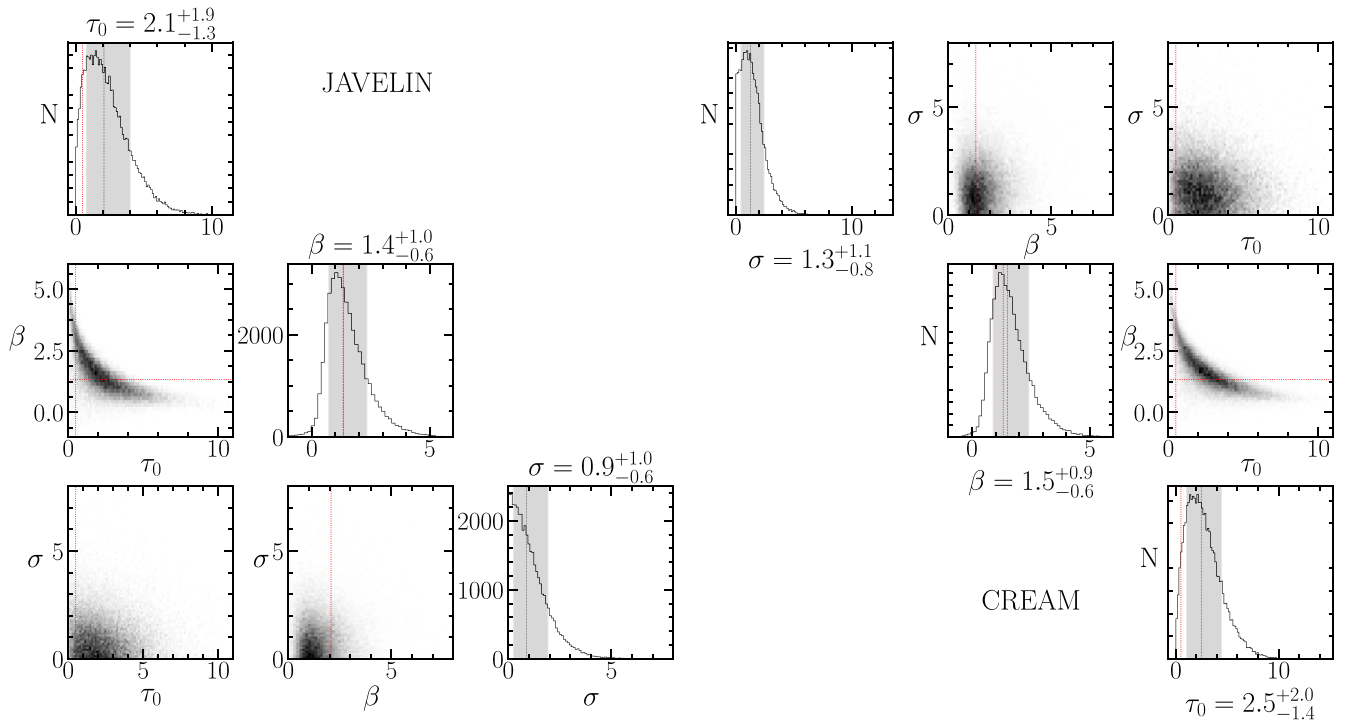


Figure 10. Posterior distribution of disk-size normalization τ_0 , wavelength scaling β , and excess scatter σ reverberation lags measured from JAVELIN (left) and CREAM (right). The red dotted lines show the prior for each parameter and the black dotted line illustrates the best-fit value computed from the median of the posteriors. The gray shaded region shows the 16th to 84th percentiles for each parameter. Using our nonlinear regression fit, we find disk sizes that are larger than the SS73 expectation and a wavelength scaling that is consistent with $\propto \lambda^{4/3}$. The fit has $\sigma = 0.9^{+1.0}_{-0.6}$ day scatter when using JAVELIN and $1.3^{+1.1}_{-0.8}$ days when using the CREAM measurements.

Li et al. (2021) show that this magnetic-coupling model is consistent with observations of the full sample of disk lags, with lower-luminosity AGNs typically having longer lags. The luminosity distributions of our samples are broad enough that we cannot conclusively test this theory. Our sample of AGN UV–optical lags has a mean of $\log(\lambda L_{3000}) = 44.3 \pm 0.5$, while the significant optical–optical lags from the sample’s parent population in Homayouni et al. (2019) have a mean of $\log(\lambda L_{3000}) = 44.4 \pm 0.6$. More measurements across a wide range of luminosities are needed to test the theory of Li et al. (2021).

5.2. Accretion-disk Temperature Profile

The standard thin-disk model (see Equation (6)) predicts an accretion-disk structure, which can be probed by the irradiated wavelength corresponding to the measured lag, as $\tau \propto \lambda^{4/3}$. Our UV–optical lags can probe this wavelength scaling, where the measured lags target different regions of the accretion disk in the quasar rest frame.

We fit Equation (9) to the observed lags reported in Table 4, allowing the disk-size normalization, τ_0 , and wavelength scaling, β , to be free parameters. We adopt a bounded normal prior for the disk-fit parameters τ_0 and β . Similar to Section 5.1, we assume the likelihood Students’ T-distribution (see Section 5), with three degrees of freedom ($\nu = 2$) centered at the measured lag. The fit also allows for an excess scatter. We use a half-Cauchy distribution to simultaneously fit σ_{Excess} in our nonlinear regression fitting approach.

Figures 10 and 11 show the result of our fits for both disk size and temperature profile. Using JAVELIN significant lags,

we find smaller best-fit values compared to the fit reported in Section 5.1, though consistent within the 1σ error bar. The disk size, $\tau_0 = 2.1^{+1.9}_{-1.3}$ days, is a factor of ~ 4 larger than the SS73 model expectation. We find a best-fit temperature scaling of $\beta = 1.4^{+1.0}_{-0.6}$. As for significant CREAM lag measurements, we find $\tau_0 = 2.5^{+2.0}_{-1.4}$ days (a factor of ~ 5 larger than SS73 model expectation) and $\beta = 1.5^{+0.9}_{-0.6}$. Using our two methods of lag analysis, we find the best-fit value for the wavelength scaling is consistent with the standard thin-disk model approximation of $\beta = 4/3$. We additionally find an excess scatter of ~ 1 day (see Figure 10), which corresponds to any unknown sources of scatter, likely related to the bolometric correction/radiative efficiency. Also, Figure 12 shows the posterior predictive distribution in connection to M_{BH} .

Similar to Section 5.1, we adopt λL_{3000} as a proxy for \dot{M}_{BH} . However, $\dot{M}_{\text{BH}} = L_{\text{Bol}}/\eta c^2 = C_{\text{Bol}} \lambda L_{3000}/\eta c^2$ probably includes the largest source of uncertainty in fitting an accretion-disk model, with 0.5 dex scatter for conversion from λL_{3000} to \dot{M}_{BH} (Richards et al. 2006; Runnoe et al. 2012). Furthermore, the efficiency η is commonly adopted to be 0.1 for highly accreting quasars (e.g., Soltan 1982). However, individual quasars are likely to have a large range of efficiencies (Davis & Laor 2011; Sun et al. 2015). Here, we use our two-parameter posteriors to obtain a distribution for the C_{Bol}/η ratio. We use the τ_0 posterior and Equation (8) to obtain the C_{Bol}/η posterior. In general, our disk measurements are not sufficient to constrain the accretion-rate conversion parameters. Our result is broadly consistent (within 1σ) with the empirical value of $C_{\text{Bol}} = 5.15$ and $\eta = 10\%$, but the posterior distribution has a long tail that is not particularly constraining on the allowed C_{Bol}/η .

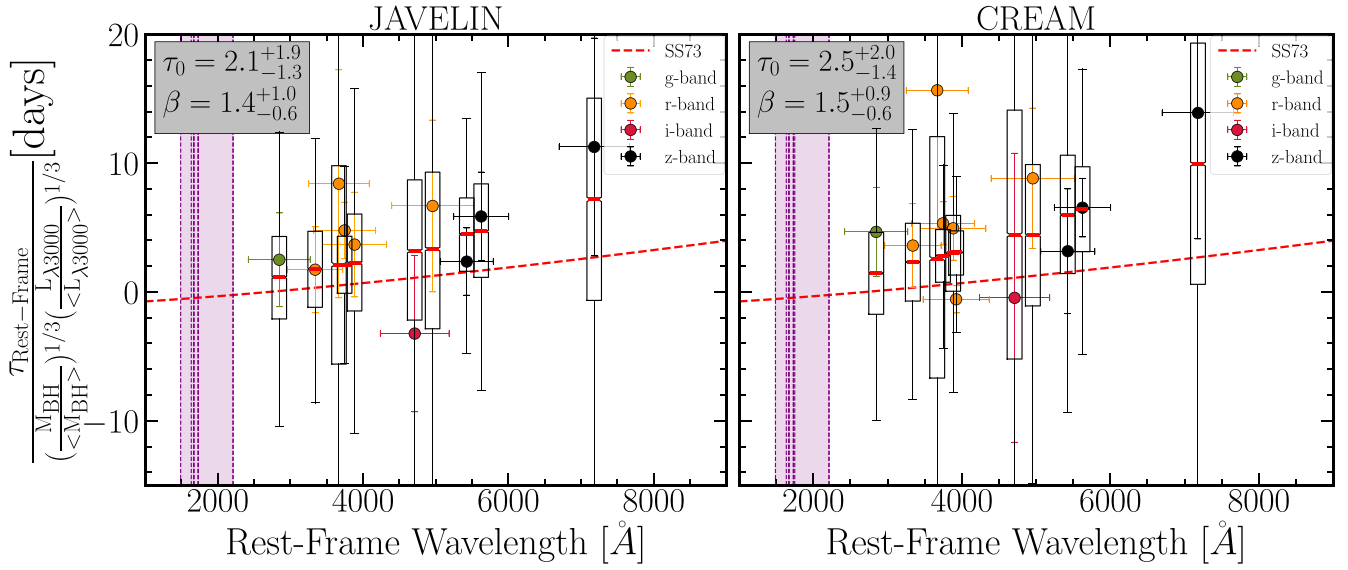


Figure 11. Rest-frame lags normalized by the ratio of M_{BH} and λL_{3000} vs. wavelength, with a best-fit line that allows both τ_0 and β to be free parameters (analogous to the τ_0 -only best-fit line in Figure 8), except here we have allowed both τ_0 and β to be free parameters. The red shaded region shows the SS73 expectation for the minimum and maximum of our sample's M_{BH} and \dot{M}_{BH} .

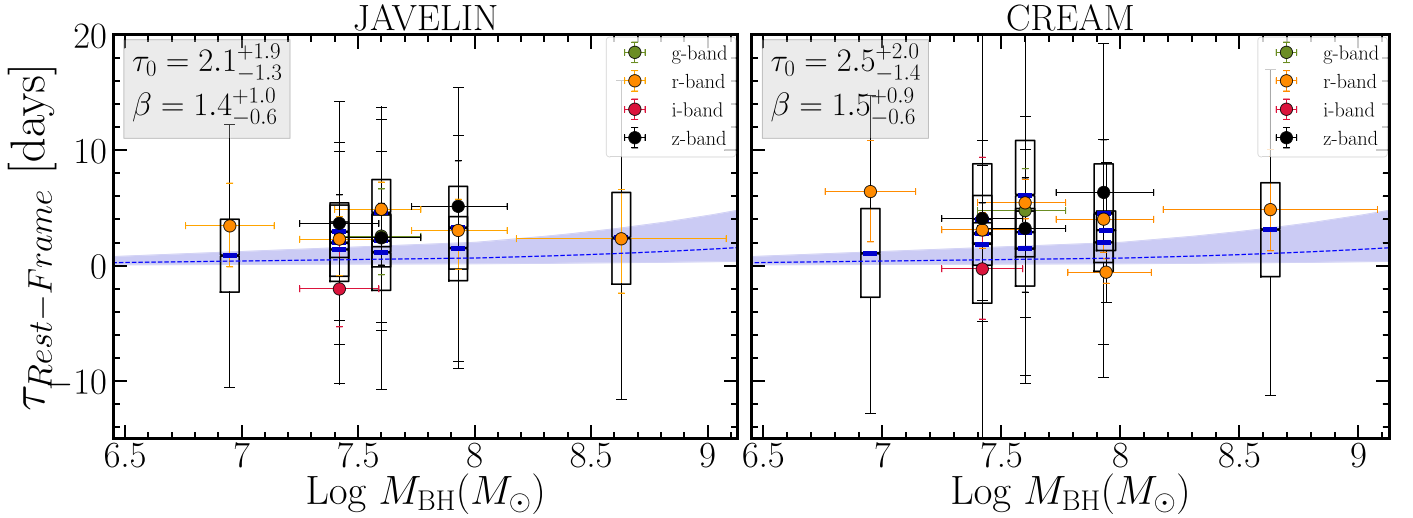


Figure 12. Accretion-disk lags as a function of M_{BH} . Here we use the posterior predictive distribution, shown as box plots, to predict how well the data match the best-fit model. The blue dashed line illustrates the SS73 model expectation as a function of M_{BH} for mean monochromatic luminosity, λL_{3000} , mean inner-disk wavelength, λ_{UV} , and mean outer-disk wavelength, λ_{opt} . We have overlapping box plots due to multiple measurements of disk lags for the same target. Even though we have few targets to allow the M_{BH} exponent in Equation (6) to be a free parameter, we test whether the two-parameter fit shows any variation with changing M_{BH} . The posterior predictive distribution reports consistent lags for different M_{BH} measurements, consistent with both no M_{BH} dependence and $M_{\text{BH}}^{1/3}$.

5.3. Disk-size Dependence on M_{BH} and λL_{3000}

To go beyond a fit that is limited to disk-size normalization and wavelength scaling, we perform a nonlinear regression to fit for the relationship between the disk size, M_{BH} , and λL_{3000} . We examine if the measured continuum lag depends on M_{BH} and \dot{M}_{BH} , as expected for the SS73 model, by fitting a nonlinear MCMC regression in three different and independent steps. First, we test for connections to M_{BH} by fixing $\dot{M}^{1/3}$ (i.e., $\lambda L_{3000}^{1/3}$) and fit Equation (9) for $\tau_{0,\text{SS73}}$ and β while allowing the M_{BH} exponent to be a free parameter, M_{BH}^γ :

$$\tau = \tau_0 \left[\left(\frac{\lambda_{\text{opt}}}{2700\text{\AA}} \right)^\beta - \left(\frac{\lambda_{\text{uv}}}{2700\text{\AA}} \right)^\beta \right] \times \left(\frac{M_{\text{BH}}}{\langle M_{\text{BH}} \rangle} \right)^\gamma \left(\frac{\lambda L_{3000}}{\langle \lambda L_{3000} \rangle} \right)^{1/3}. \quad (10)$$

Second, we fit for a dependence of disk lags on $\tau_{0,\text{SS73}}$, β , and the accretion rate while fixing the M_{BH} exponent to the SS73 expectation, $M_{\text{BH}}^{1/3}$ and allow the dependence of the disk size

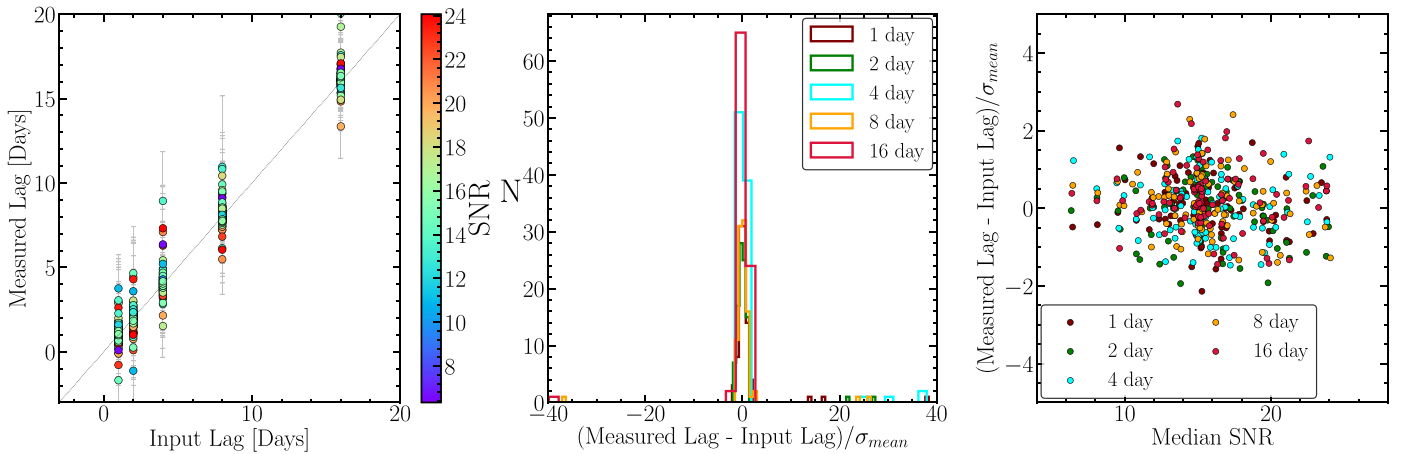


Figure 13. Left: the comparison between the measured and input lags from 500 simulated lightcurves, color-coded by the median S/N of the lightcurve fluxes. The synthetic lightcurves have added noise from our optical photometry observations. We test different input lags similar to expected accretion-disk lag values. Overall, we find that our measured lags are consistent with the median of each distribution overlapping with the 1:1 line. Middle: the distribution of lag difference divided by the JAVELIN uncertainties illustrated by a different color for each of the input lags. The breakdown for each individual lag shows that we find that the measured lag is consistent within $<1\sigma$ for 66%–68% of the simulations. We also find that the measured and input lags are consistent within $<2\sigma$ for 92%–96% of the simulations. Thus, we find there is no bias in the measured lag and the estimated lag uncertainties are accurate. Right: distribution of the lag difference weighted by lag uncertainties as a function of the median lightcurve S/N. Here we use similar color-coding to the middle panel to illustrate the different input lags. For a clearer display of the results, the plot limits exclude the 4% of cases where the lag differences are discrepant by more than 5σ .

Table 5
Fits to Black Hole Mass and λL_{3000}

Free Parameters	τ_0	β	γ	δ	σ
τ_0, β, γ	$1.7^{+1.9}_{-1.2}$	$1.3^{+1.1}_{-0.7}$	$0.3^{+0.9}_{-0.8}$	fixed (1/3)	$0.9^{+1.1}_{-0.7}$
τ_0, β, δ	$1.8^{+1.9}_{-1.2}$	$1.1^{+1.0}_{-0.6}$	fixed (1/3)	$0.3^{+1.0}_{-0.5}$	$1^{+1.1}_{-0.7}$
τ_0, γ, δ	$1.3^{+2.0}_{-1}$	fixed(4/3)	$0.3^{+1.5}_{-1.0}$	$0.6^{+1.6}_{-0.8}$	$1.1^{+1.2}_{-0.7}$

with observable luminosity, λL_{3000} , be a free parameter λL_{3000}^δ as

$$\tau = \tau_0 \left[\left(\frac{\lambda_{\text{opt}}}{2700\text{\AA}} \right)^\beta - \left(\frac{\lambda_{\text{uv}}}{2700\text{\AA}} \right)^\beta \right] \times \left(\frac{M_{\text{BH}}}{\langle M_{\text{BH}} \rangle} \right)^{1/3} \left(\frac{\lambda L_{3000}}{\langle \lambda L_{3000} \rangle} \right)^\delta. \quad (11)$$

Finally, in the third step of our fit, we allow both the M_{BH} and λL_{3000} exponents to be free parameters (i.e., $\tau \propto M_{\text{BH}}^\gamma \lambda L_{3000}^\delta$) with fixed $\beta = 4/3$ as expected from SS73 and from our two-parameter fit in Section 5.2. We follow an independent and step-by-step approach to fitting to build better intuition and avoid overinterpreting multiparameter fits with large uncertainties, given our small sample size and the large uncertainties associated with η and C_{bol} .

Our set of black hole masses is obtained from RM H β masses (Grier et al. 2017) and only one of our targets, RM824, has its black hole mass measured using the single-epoch method (Shen et al. 2019). To perform the nonlinear MCMC regression for the three-parameter fit, with $\tau_{0,\text{SS73}}$, β , and γ , we provide the M_{BH} prior as a normal distribution centered at the measured M_{BH} with uncertainties as the width from Table 1. To perform the three-parameter fit that includes $\tau_{0,\text{SS73}}$, β , and δ , we incorporate only the λL_{3000} measurements and uncertainties as a normal distribution prior. Similar to previous discussions in Sections 5.1 and 5.2, we report an excess scatter, σ , for the fit. Table 5 provides a brief summary of these different fitting approaches using the JAVELIN lags results. In general, we find

that the best-fit values are consistent with theoretical SS73 expectations, but with large uncertainties that are similarly consistent with a wide range of relationships between disk size, black hole mass, and accretion rate. The three-parameter fit involving both M_{BH} and λL_{3000} shows the highest scatter.

6. Summary

We have presented results from an intensive UV–optical photometric monitoring campaign of eight SDSS-RM quasars. The selected sample has the advantages of a wide range of Eddington ratios and reliable black hole masses from the first year of the SDSS-RM monitoring program (Grier et al. 2017). Our study of UV–optical disk measurement is the first study to go beyond $z > 0.3$. Our set of UV lightcurves have an every-other-day (2 day) cadence from HST UVIS F275W and coordinated ground-based monitoring for up to four optical bands over three months of monitoring. We use these sets of photometric lightcurves to measure UV–optical continuum lags and to study the accretion-disk structure and its connection to accretion rate. We report UV–optical lag results from two lag-identification methods, JAVELIN and CREAM. We use statistical criteria to ensure that we select significant lags that are arising from physical reverberation. Our main results are as follows:

1. Significant continuum lags are detected between the UV at $\lambda 2704$ and the optical broadband g , r , i , and z filters at 4686, 6166, 7480, 8932 Å. Due to lag-significance criteria, not all four interband lags were found to be significant measurements for every target (with some limitations due to observation design). In general, the time delay observation

is found to be consistent with a disk-stratification model where $\tau_{uv-g} < \tau_{uv-r} < \tau_{uv-i} < \tau_{uv-z}$.

2. We find an excess of large lags (rest-frame lags $> +10$ days and < -10 days) that overlap with the diffuse Balmer continuum window at $\lambda 3500\text{--}3900$ and the diffuse iron continuum windows at $\lambda 4434\text{--}4684$ and $\lambda 5100\text{--}5477$. These outlier lags are a factor of ≈ 2.5 larger than the mean JAVELIN significant lags of 2.8 days and a factor of ≈ 3.8 times larger than mean CREAM significant lags of 3.8 days. We additionally have one source with a long lag that is associated with significant contamination from the $H\alpha$ emission line.
3. The best-fit UV–optical disk-size normalization is found to be consistently larger than the SS73 theoretical expectation in all three fitting approaches. From the simple one-parameter fit, we found disk sizes that are $\sim 4\text{--}6$ times larger than the SS73 expectation of 0.5 days. Using the two-parameter fitting approach, we found disk normalizations that are $\sim 4\text{--}5$ times larger, and finally, from the three-parameter fits, we found disk-size normalizations that are $\sim 2\text{--}3$ times larger than the standard thin-disk model, assuming $\chi = 2.49$. However, larger disks can also be explained by the larger $\chi = 4.97$ for a single flux annulus and could reduce these differences by half.
4. We show that our UV–optical lags are consistent with the optical–optical lags as measured previously for the same quasars (Homayouni et al. 2019). Our quasars are selected from a broad diversity of the SS73 disk sizes, and these measurements are consistent with being drawn from the high-lag portion of the SDSS-RM sample.
5. The trend of increasing lag as a function of wavelength is consistent with the standard thin-disk expectation of $\tau \propto \lambda^{4/3}$. We found a best-fit value for the wavelength scaling $\beta = 1.4_{-0.6}^{+1}$ using the JAVELIN method and a slightly larger but consistent $\beta = 1.5_{-0.6}^{+0.9}$ using CREAM measurements.
6. Assuming that continuum lags scale with black hole mass as $\tau \propto \tau_0 M_{\text{BH}}^\gamma$, $\tau \propto \tau_0 \lambda L_{3000}^\delta$ and $\tau \propto \tau_0 M_{\text{BH}}^\gamma \lambda L_{3000}^\delta$, we examined the dependency upon M_{BH} and λL_{3000} from three different fitting approaches. We found that the disk size is connected to M_{BH} consistent with the SS73 expectation (i.e., the power-law slope of 1/3). We found the dependence to λL_{3000} is also consistent with the theoretical value from SS73; however, the best-fit values for mass and luminosity dependence have higher uncertainty and excess scatter when they are simultaneously allowed to be a free parameter in the fit.

Our new measurements represent a new advance in “industrial-scale” multiobject UV–optical accretion-disk-size measurements from HST observations. Our measured disk sizes are broadly consistent with the SS73 disk model. We demonstrate that fitting only the disk normalization results in larger disks by a factor of $\sim 5\text{--}6$ while fitting a comprehensive accretion disk including the color profile and mass and luminosity results in disks that are ~ 2 times larger, although with larger uncertainties. This motivates future work to better measure bolometric luminosity and radiative efficiency alongside accretion-disk sizes and black hole mass.

Y.H., J.R.T., and G.F.A. acknowledge support from NASA grants HST-GO-15650 and 18-2ADAP18-0177 and NSF grant CAREER-1945546. K.H. acknowledges support from STFC

grant ST/R000824/1. C.J.G. acknowledges support from NSF grant AST-2009949. Y.S. acknowledges support from NSF grants AST-1715579 and AST-2009947. P.H. acknowledges support from the Natural Sciences and Engineering Research Council of Canada (NSERC), funding reference number 2017-05983. L.C.H. was supported by the National Science Foundation of China (11721303, 11991052) and the National Key R&D Program of China (2016YFA0400702).

Software: CREAM (Starkey et al. 2016), Javelin (Zu et al. 2011), PyceCREAM (<https://github.com/dstarkey23/pycecream>), PyMc3 (<https://docs.pymc.io/notebooks/-GLM-robust.html>).

Appendix

Our coordinated ground-based observations (see Section 2.3) have flux measurements with a median S/N of ~ 16 , where a typical variation of S/N is ~ 3 for our set of lightcurves. Here we assess the effects of the lightcurve S/N on lag recovery rate using simulated lightcurves.

To generate our synthetic optical lightcurves, we start from the JAVELIN DRW modeled UV lightcurve for our sample of significant JAVELIN lags in Table 4. For each optical lightcurve simulation, we assign typical noise to the DRW model, where the noise is drawn from a random normal distribution with the median and NAMD of the observed lightcurves S/N. At each epoch, we resample the flux using a Gaussian normal distribution with the model mean flux and a dispersion equal to the flux uncertainty determined by the noise. We scale the synthetic lightcurve variance to match the rms variability of the observed lightcurves. To mimic the UV–optical lag, we shift the optical lightcurves by representative accretion-disk lags of 1, 2, 4, 8, and 16 days. To realistically model the responding optical lightcurves with a broader disk response, we convolve these optical lightcurves with a Gaussian kernel with widths that are 20% of the input lags. This accounts for the wavelength-dependent aspect of the transfer function as demonstrated by Starkey et al. (2016) where the longer wavelength response has a broader transfer function. Finally, the synthetic lightcurves are downsampled to have a similar cadence to the observed cadence reported in Table 2. To incorporate the effects of the nonuniform noise due to lunation, we downsample the simulated lightcurves by selecting only the epochs that match the observed epochs. We then add the actual observed flux uncertainty to each simulated data point to capture similar flux uncertainties as was observed for our optical lightcurves. We simulate $N = 10$ times per target and bandpass, totaling 500 simulated optical lightcurves.

Similarly, we generate the simulated UV lightcurves from the DRW models, resampling the flux using a random normal distribution with the model flux and a dispersion equal to the square root of the sum of representative UV-lightcurve noise and the model uncertainty squared.


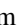










Finally, we downsample the UV lightcurve using the total number of subexposures in the HST observations (see Table 2).

We then use JAVELIN to compute the UV–optical lag between each pair of UV and optical lightcurves, with damping timescale and transfer-function width as described in Section 4.2. After we compute all lags for the simulated lightcurves, we identify the significant lags using the lag reliability criteria discussed in Section 4.4.

In the end, we measured 478 significant lags from 500 synthetic UV–optical lightcurve set in Table 4. Figure 13

compares the input and recovered lags for the significant lag measurements. We find that the synthetic lightcurves have lags that are statistically consistent with the input lags. Our simulations reveal that the measured and input lags are consistent for 66%–68% within $<1\sigma$ and also similarly consistent within $<2\sigma$ for 92%–96% of the simulations. We find no bias in lag measurement caused by the S/N in the optical lightcurves. We also conclude that the estimated lag uncertainties are reliable because they accurately describe the differences between the input and measured lags.

ORCID iDs

Y. Homayouni  <https://orcid.org/0000-0002-0957-7151>
 Megan R. Sturm  <https://orcid.org/0000-0003-1055-1888>
 Jonathan R. Trump  <https://orcid.org/0000-0002-1410-0470>
 Keith Horne  <https://orcid.org/0000-0003-1728-0304>
 C. J. Grier  <https://orcid.org/0000-0001-9920-6057>
 Yue Shen  <https://orcid.org/0000-0003-1659-7035>
 W. N. Brandt  <https://orcid.org/0000-0002-0167-2453>
 P. B. Hall  <https://orcid.org/0000-0002-1763-5825>
 Luis C. Ho  <https://orcid.org/0000-0001-6947-5846>
 Jennifer I-Hsiu Li  <https://orcid.org/0000-0002-0311-2812>
 Mouyuan Sun  <https://orcid.org/0000-0002-0771-2153>
 D. P. Schneider  <https://orcid.org/0000-0001-7240-7449>

References

- Bentz, M. C., & Katz, S. 2015, *PASP*, 127, 67
 Blandford, R. D., & McKee, C. F. 1982, *ApJ*, 255, 419
 Boroson, T. A., & Green, R. F. 1992, *ApJS*, 80, 109
 Bradley, L., Sipocz, B., Robitaille, T., et al. 2017, *Astropy/Photutils: V0.4*, v0.4, Zenodo, doi:10.5281/zenodo.1039309
 Bramich, D. M. 2008, *MNRAS*, 386, L77
 Bruhweiler, F., & Verner, E. 2008, *ApJ*, 675, 83
 Cackett, E. M., Chiang, C.-Y., McHardy, I., et al. 2018, *ApJ*, 857, 53
 Cackett, E. M., Gelbord, J., Li, Y.-R., et al. 2020, *ApJ*, 896, 1
 Cackett, E. M., Horne, K., & Winkler, H. 2007, *MNRAS*, 380, 669
 Chan, J. H. H., Millon, M., Bonvin, V., & Courbin, F. 2020, *A&A*, 636, A52
 Chelouche, D. 2013, *ApJ*, 772, 9
 Chelouche, D., & Zucker, S. 2013, *ApJ*, 769, 124
 Collier, S., Crenshaw, D. M., Peterson, B. M., et al. 2001, *ApJ*, 561, 146
 Collier, S. J., Horne, K., Kaspi, S., et al. 1998, *ApJ*, 500, 162
 Davis, S. W., & Laor, A. 2011, *ApJ*, 728, 98
 Edelson, R., Gelbord, J., Cackett, E., et al. 2017, *ApJ*, 840, 41
 Edelson, R., Gelbord, J., Cackett, E., et al. 2019, *ApJ*, 870, 123
 Edelson, R., Gelbord, J. M., Horne, K., et al. 2015, *ApJ*, 806, 129
 Fausnaugh, M. M., Denney, K. D., Barth, A. J., et al. 2016, *ApJ*, 821, 56
 Fausnaugh, M. M., Starkey, D. A., Horne, K., et al. 2018, *ApJ*, 854, 107
 Galeev, A. A., Rosner, R., & Vaiana, G. S. 1979, *ApJ*, 229, 318
 Gelman, A., & Rubin, D. B. 1992, *StaSc*, 7, 457
 Gonzaga, S. 2012, *The DrizzlePac Handbook* (Baltimore, MD: STScI)
 Grier, C. J., Shen, Y., Horne, K., et al. 2019, *ApJ*, 887, 38
 Grier, C. J., Trump, J. R., Shen, Y., et al. 2017, *ApJ*, 851, 21
 Homayouni, Y., Trump, J. R., Grier, C. J., et al. 2019, *ApJ*, 880, 126
 Homayouni, Y., Trump, J. R., Grier, C. J., et al. 2020, *ApJ*, 901, 55
 Jiang, Y.-F., Green, P. J., Greene, J. E., et al. 2017, *ApJ*, 836, 186
 Kammoun, E. S., Papadakis, I. E., & Dovčiak, M. 2021, *MNRAS*, 503, 4163
 Kelly, B. C., Bechtold, J., & Siemiginowska, A. 2009, *ApJ*, 698, 895
 Korista, K. T., & Goad, M. R. 2001, *ApJ*, 553, 695
 Korista, K. T., & Goad, M. R. 2019, *MNRAS*, 489, 5284
 Kozłowski, S. 2016, *ApJ*, 826, 118
 Kriss, G. A., Peterson, B. M., Crenshaw, D. M., & Zheng, W. 2000, *ApJ*, 535, 58
 Krolik, J. H., Horne, K., Kallman, T. R., et al. 1991, *ApJ*, 371, 541
 Kuehn, C. A., Baldwin, J. A., Peterson, B. M., & Korista, K. T. 2008, *ApJ*, 673, 69
 Lawther, D., Goad, M. R., Korista, K. T., Ulrich, O., & Vestergaard, M. 2018, *MNRAS*, 481, 533
 Li, J., Shen, Y., Brandt, W. N., et al. 2019, *ApJ*, 884, 119
 Li, T., Sun, M., Xu, X., et al. 2021, *ApJL*, 912, L29
 MacLeod, C. L., Ivezić, Ž., Kochanek, C. S., et al. 2010, *ApJ*, 721, 1014
 MacLeod, C. L., Ivezić, Ž., Sesar, B., et al. 2012, *ApJ*, 753, 106
 Maronna, R. A., Martin, R. D., & Yohai, V. J. 2006, *Robust Statistics* (New York: John Wiley & Sons Ltd)
 McHardy, I. M., Cameron, D. T., Dwelly, T., et al. 2014, *MNRAS*, 444, 1469
 McHardy, I. M., Connolly, S. D., Horne, K., et al. 2018, *MNRAS*, 480, 2881
 Momcheva, I. G., van Dokkum, P. G., van der Wel, A., et al. 2017, *PASP*, 129, 015004
 Morgan, C. W., Hyer, G. E., Bonvin, V., et al. 2018, *ApJ*, 869, 106
 Mowla, L. A., van Dokkum, P., Brammer, G. B., et al. 2019, *ApJ*, 880, 57
 Mudd, D., Martini, P., Zu, Y., et al. 2018, *ApJ*, 862, 123
 Mushotzky, R. F., Edelson, R., Baumgartner, W., & Gandhi, P. 2011, *ApJL*, 743, L12
 Pahari, M., McHardy, I. M., Vincentelli, F., et al. 2020, *MNRAS*, 494, 4057
 Peterson, B. M. 1993, *PASP*, 105, 247
 Peterson, B. M., Ferrarese, L., Gilbert, K. M., et al. 2004, *ApJ*, 613, 682
 Read, S. C., Smith, D. J. B., Jarvis, M. J., & Gürkan, G. 2020, *MNRAS*, 492, 3940
 Reynolds, C. S., & Nowak, M. A. 2003, *PhR*, 377, 389
 Richards, G. T., Lacy, M., Storrie-Lombardi, L. J., et al. 2006, *ApJS*, 166, 470
 Runnoe, J. C., Brotherton, M. S., & Shang, Z. 2012, *MNRAS*, 426, 2677
 Salvatier, J., Wiecki, T. V., & Fonnesbeck, C. 2016, *PyMC3: Python probabilistic programming framework*, *Astrophysics Source Code Library*, ascl:1610.016
 Sergeev, S. G., Doroshenko, V. T., Golubinskiy, Y. V., Merkulova, N. I., & Sergeeva, E. A. 2005, *ApJ*, 622, 129
 Shakura, N. I., & Sunyaev, R. A. 1973, *A&A*, 500, 33
 Shappee, B. J., Prieto, J. L., Grupe, D., et al. 2014, *ApJ*, 788, 48
 Shen, Y., Brandt, W. N., Dawson, K. S., et al. 2015, *ApJS*, 216, 4
 Shen, Y., Hall, P. B., Horne, K., et al. 2019, *ApJS*, 241, 34
 Shen, Y., Horne, K., Grier, C. J., et al. 2016, *ApJ*, 818, 30
 Soltan, A. 1982, *MNRAS*, 200, 115
 Starkey, D., Horne, K., Fausnaugh, M. M., et al. 2017, *ApJ*, 835, 65
 Starkey, D. A., Horne, K., & Villforth, C. 2016, *MNRAS*, 456, 1960
 Sun, M., Trump, J. R., Shen, Y., et al. 2015, *ApJ*, 811, 42
 Sun, M., Xue, Y., Brandt, W. N., et al. 2020, *ApJ*, 891, 178
 van Dokkum, P. G. 2001, *PASP*, 113, 1420
 Vanden Berk, D. E., Richards, G. T., Bauer, A., et al. 2001, *AJ*, 122, 549
 Vestergaard, M., & Wilkes, B. J. 2001, *ApJS*, 134, 1
 Wanders, I., Peterson, B. M., Alloin, D., et al. 1997, *ApJS*, 113, 69
 Yu, Z., Martini, P., Davis, T. M., et al. 2020, *ApJS*, 246, 16
 Zu, Y., Kochanek, C. S., & Peterson, B. M. 2011, *ApJ*, 735, 80